



UNIVERSITY OF LEEDS

This is a repository copy of *Development and long-term evolution of density staircases in stirred stratified turbulence*.

White Rose Research Online URL for this paper:

<https://eprints.whiterose.ac.uk/190853/>

Version: Accepted Version

Article:

Pružina, P, Hughes, DW orcid.org/0000-0002-8004-8631 and Pegler, SS (2022)

Development and long-term evolution of density staircases in stirred stratified turbulence.

Physical Review Fluids, 7 (10). 104801. ISSN 2469-990X

<https://doi.org/10.1103/PhysRevFluids.7.104801>

©2022 American Physical Society. This is an author produced version of an article accepted for publication in Physical Review Fluids. Uploaded in accordance with the publisher's self-archiving policy.

Reuse

See Attached

Takedown

If you consider content in White Rose Research Online to be in breach of UK law, please notify us by emailing eprints@whiterose.ac.uk including the URL of the record and the reason for the withdrawal request.



eprints@whiterose.ac.uk
<https://eprints.whiterose.ac.uk/>

Development and long-term evolution of density staircases in stirred stratified turbulence

Paul Pružina,* David W. Hughes, and Samuel S. Pegler
School of Mathematics, University of Leeds, Leeds LS2 9JT, UK
(Dated: September 5, 2022)

We formulate and analyse a model describing the development and evolution of density staircases in stratified turbulence, using it to investigate the long-term evolution and merger of layers and demonstrating an inverse logarithmic relationship for their decay. Starting from the Boussinesq equations, including viscous stresses and density diffusion, we use spatial averaging and simple closure assumptions to derive a system of equations describing the evolution of the density profile of a turbulent stratified fluid in terms of the horizontally averaged buoyancy and turbulent kinetic energy. Subject to critical conditions on the buoyancy gradient, the model predicts the development of a system of well-mixed layers separated by sharp interfaces. A linear stability analysis determines critical conditions for layer formation, and demonstrates both a minimum and maximum initial density gradient necessary for layering. Increasing the viscosity decreases the maximum unstable wavenumber, thereby increasing the vertical lengthscale of layers. Increasing the diffusivity has a similar effect, but can also suppress the instability entirely by decreasing the unstable range of gradients. The long-term nonlinear evolution shows that the layers undergo successive mergers, with each merger increasing the magnitude of steps in the density staircase. In particular, by applying boundary conditions of fixed buoyancy, instead of the previously adopted condition of zero buoyancy flux, we reduce the influence of the boundaries at late times, allowing us to investigate the long-term evolution of layer mergers in stratified turbulence in detail for the first time. For long times t , we infer a general law describing the evolution of the number of layers N as $1/N \sim \log t$, suggesting a self-similar structure to merger dynamics, and a link to Cahn-Hilliard models of layering.

I. INTRODUCTION

The dynamics of stratified turbulent flows presents a rich variety of behaviour. One of the most striking examples is the spontaneous development of density staircases: given an initially uniform density gradient, stirring the fluid can lead to the formation of well-mixed layers, in which the density is nearly constant, separated by sharp interfaces with strong density gradients. These layers are long-lasting, and show little variation across wide horizontal areas. The interfaces are narrow, but the density field across them is smooth, with a well-defined finite thickness. Experimental work has produced such layered structures by dragging a rod or grid back and forth through an initially stable gradient of salt concentration [1–3].

One of the fascinating aspects of staircase formation is its appearance in a number of ostensibly different areas of physics. In an atmospheric context, rotating stratified flow can give rise to a potential vorticity staircase, which manifests as strong zonal jets, such as the bands in Jupiter’s atmosphere [4, 5]. In double-diffusive convection — a phenomenon of both geophysical and astrophysical importance — layered structures can arise in both the fingering and diffusive regimes, being observed both oceanographically [6, 7] and in numerical simulations [8–11]. In the context of hot magnetised plasmas, turbulence can generate permeable localised transport barriers that globally organise into the so-called ‘ $\mathbf{E} \times \mathbf{B}$ staircase’; this was first established through gyro-kinetic simulations [12] and later confirmed experimentally [13]. The formation of layers is *anti-diffusive*, with up-gradient transport, and so represents behaviour contrary to the naively expected case of homogenisation. Understanding how layers can form, and how they evolve over time, is clearly therefore a problem of considerable implicit scientific interest. Furthermore, layered systems exhibit very different transport properties to those of familiar weakly inhomogeneous systems [see, for example, 10, 11]. Thus, understanding the physics of layering is also crucial to developing an accurate description of transport in oceanographic and atmospheric flows, in stellar interiors and in magnetically-confined plasmas.

Early work on layering in stratified fluids by Phillips [14] and Posmentier [15] proposed a mechanism for the development of staircases based on the turbulent diffusion of buoyancy, with a diffusion coefficient that could be negative. Specifically, Posmentier modelled the evolution of the buoyancy profile $b(z, t) = (\rho_0 - \rho)g/\rho_0$ (where ρ is the fluid density, ρ_0 a reference density, and g the gravitational acceleration) by the one-dimensional diffusion equation

$$b_t = [f(b_z)]_z = f'(b_z)b_{zz}, \quad (1)$$

* mmpep@leeds.ac.uk

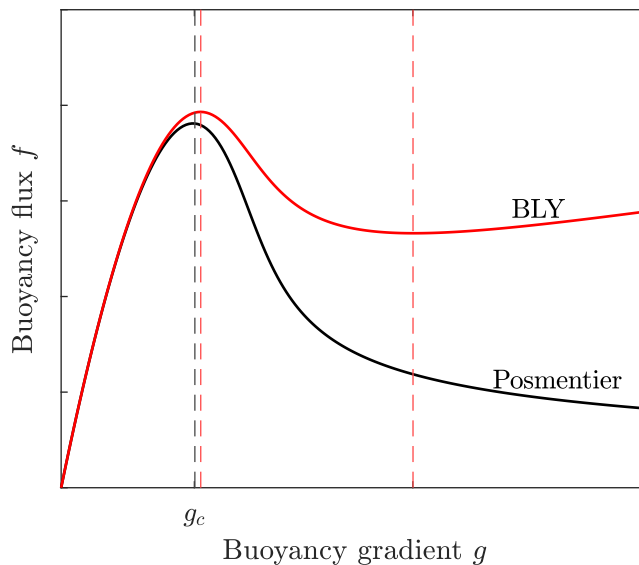


FIG. 1. The solid lines show the flux-gradient relations used by Posmentier (black) and BLY (red). The black dashed line shows the minimum value $g = g_c$ for which Posmentier’s flux satisfies the instability condition (2). The red dashed lines show the boundaries of the finite region in which the flux in the BLY model satisfies (2).

where z is height, t is time, and the specified function $f(b_z)$ relates the local flux of buoyancy to the local buoyancy gradient b_z . Throughout, we shall use subscripts of z and t to denote partial derivatives. In the situation where the system is initialised from a state of uniform buoyancy gradient, with $b_z = g_0$ a constant (a linear stratification), the initial state is unstable if

$$f'(g_0) < 0. \quad (2)$$

If condition (2) holds, then a perturbation that increases the local buoyancy gradient b_z acts to decrease the buoyancy flux f , which further increases the buoyancy gradient through negative diffusion, in accordance with (1). Posmentier proposed a flux-gradient relation, $f(b_z)$, of the form shown in Fig. 1, such that there is a critical value g_c above which condition (2) is satisfied. For a background gradient $b_z > g_c$, a small perturbation will grow in amplitude. If the perturbation acts to increase b_z , then it may grow without constraint, as inequality (2) is satisfied for all $b_z > g_c$. However if the perturbation acts to decrease b_z , then the amplitude of the perturbation will grow only until $b_z = g_c$ locally, at which point the instability is arrested. Hence, perturbations can develop into a stepped structure, with alternating regions of large and small buoyancy gradients — a process commonly known as the ‘Phillips effect’. The argument advanced above is based on linear stability considerations and hence provides information on the initial evolution to a layered state; when the perturbations attain a sufficiently large amplitude, nonlinear dynamics will come into play. The Phillips effect has been demonstrated to lead to layering in two-dimensional stratified Boussinesq turbulence [16]. In the diffusive regime of double diffusive convection (as found in Polar oceans), the Phillips effect acting on one component of density can lead to layering without the need for double diffusive effects [17].

The model described by equation (1) provides a good starting point to describe a mechanism for layering. However, it relies on specifying the buoyancy flux function, and hence cannot give a full description of the physics from first principles, nor of the intricacies of layer evolution. For example, (1) takes no account of the impact of the buoyancy on the velocity field; nor does it provide a mechanism to arrest the steepening of the interface, meaning that the buoyancy field eventually develops discontinuities. A particular mathematical difficulty of the model is that the linearised version of (1) becomes a negative diffusion equation for b in regions where $f'(b_z) < 0$. The growth rate of perturbations therefore diverges as the wavenumber increases, causing the problem to be ill-posed.

To look beyond the initial formation of layers, and investigate their longer-term evolution, the problem needs to be regularised. One possibility is to add a time delay, so that the flux does not adjust immediately to changes in the gradient, but takes a finite time to react [18, 19]. More specifically, the flux $F(t)$ can be prescribed to depend on the buoyancy gradient $b_z(t - \tau)$, for some small delay time τ . This removes the high-wavenumber instability, but the solutions still develop discontinuities in finite time.

Balmforth, Llewellyn Smith and Young [20] (hereinafter BLY) developed a more detailed model to address these physical and mathematical issues. Using dimensional and physical arguments, they obtained the following dimension-

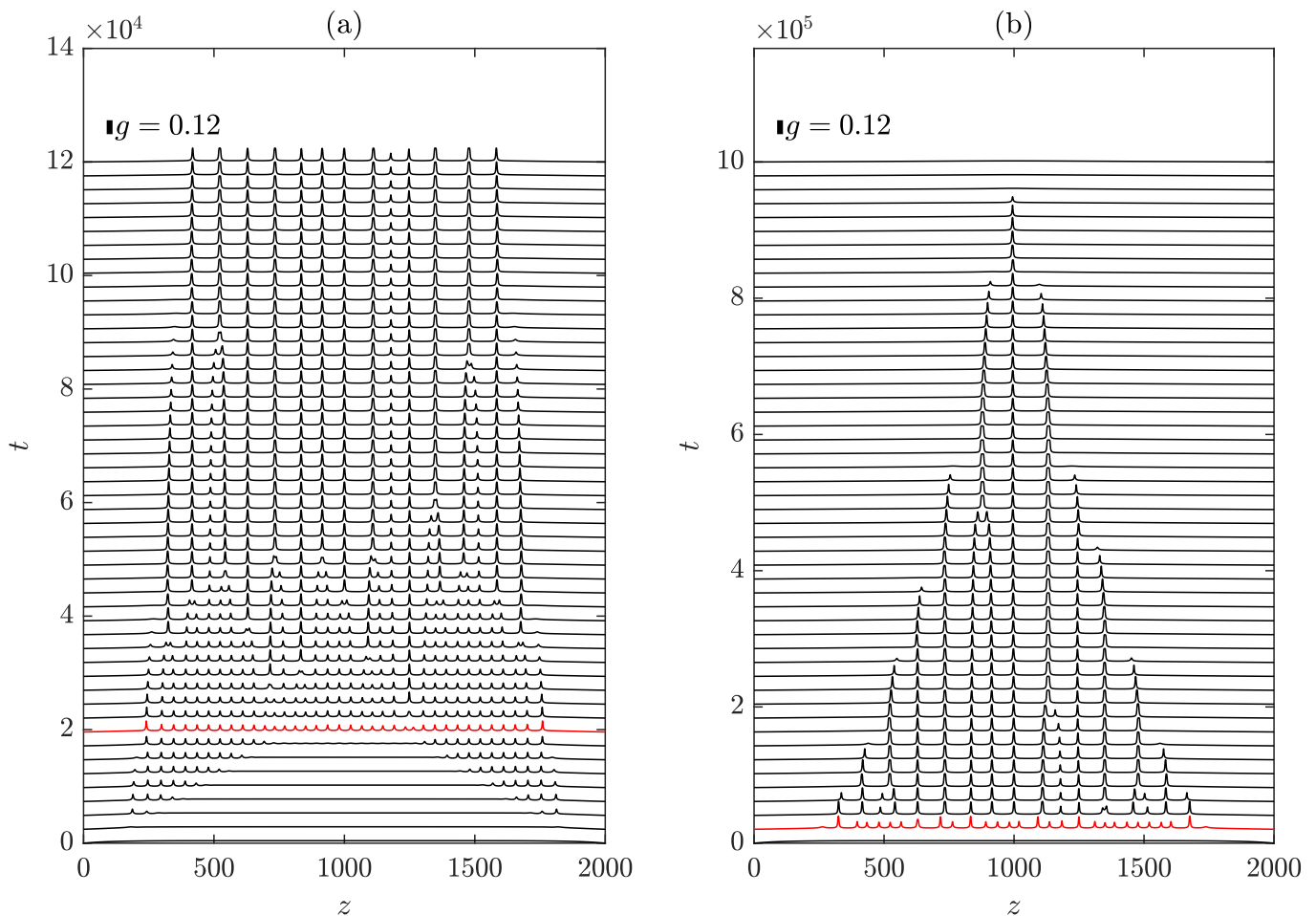


FIG. 2. Reproduction of numerical results using the BLY model (3)–(4), showing the initial development of the layered state, layer mergers, and expansion of the edge regions. The plots show the spatial profile of the dimensionless buoyancy gradient $g(z, t) = b_z(z, t)$ across the depth of the layer at regular time intervals. The scale bar at the top of the panel indicates the magnitude of g . Panel (a) reproduces the simulation of Fig. 6 of BLY, while panel (b) shows the continued long-term evolution to $t = 10^6$. The edge regions expand at a rate $\propto t^{1/2}$ into the interior, eventually destroying the entire layered region and filling the domain. In both panels, the solution at $t = 2 \times 10^4$ is shown in red; this denotes the first time at which consistent layers exist across the entire interior region.

less model for the evolution of the horizontally averaged buoyancy $b(z, t)$ and turbulent kinetic energy $e(z, t)$:

$$b_t = \left(l e^{1/2} b_z \right)_z, \quad (3)$$

$$e_t = \left(l e^{1/2} e_z \right)_z - l e^{1/2} b_z - \frac{\varepsilon e^{3/2}}{l} + P, \quad (4)$$

where $l = l(b_z, e)$ is a suitably parameterised mixing length l and $P = P(b_z, e)$ is the energy production term, for which BLY adopted the following form:

$$P = \frac{\varepsilon e^{1/2}}{l}, \quad (5)$$

where ε is a dimensionless mixing parameter. Equations (3)–(4) form a system of turbulent diffusion equations, with the first term on each right hand side representing eddy diffusion. In the energy equation (4), the second term on the right hand side is necessarily the same as the buoyancy flux on the right-hand side of (3), accounting for the transfer between potential and kinetic energy. The penultimate term in (4) describes the dissipation of turbulent kinetic energy.

The parameterisation of the lengthscale $l(b_z, e)$ is a crucial component of the model. In the initial non-layered state, the key lengthscale is that of the turbulent eddies induced by stirring, which is non-dimensionalised to unity

($l = 1$). As a result of the stirring, a shorter lengthscale emerges in regions where the buoyancy gradient is high. This is represented by the Ozmidov lengthscale $l_O = (e/b_z)^{1/2}$, defined as the characteristic size of the largest eddy that is not significantly affected by buoyancy in a stably stratified fluid [21]. The parameterisation for $l(b_z, e)$ interpolates between these two scales, taking the stirring length when the stratification is weak, and the Ozmidov length in strongly stratified regions. The particular form chosen by BLY is

$$l(b_z, e) = \frac{e^{1/2}}{(e + b_z)^{1/2}}, \quad (6)$$

which appropriately transitions from the stirring length $l \sim 1$ for $b_z \ll e$ to the Ozmidov length as $b_z \gg e$.

The system (3)–(6) is solved in the domain $0 < z < H$. BLY prescribe no-flux boundary conditions on both buoyancy and energy, as specified by

$$b_z(0, t) = b_z(H, t) = 0, \quad e_z(0, t) = e_z(H, t) = 0. \quad (7)$$

These no-flux conditions imply that the total energy is changed only by dissipation and stirring.

Models of the form (3)–(4), and extensions thereof, have been applied to a number of different physical problems in which staircases have been observed, including double diffusive convection [22] and potential vorticity staircases [23]. Three-component models of a similar form have also been formulated to study $\mathbf{E} \times \mathbf{B}$ staircases in plasma drift-wave turbulence [24–26].

The coupling of the buoyancy $b(z, t)$ to the energy $e(z, t)$ in the BLY model (3)–(4) is found to suppress the high wavenumber instability inherent in equation (1), thereby ensuring that the problem is well posed. To prevent the formation of infinite buoyancy gradients, BLY’s model specifies an N-shaped flux-gradient relation, so that condition (2) is satisfied for only a finite range of b_z . This is shown by the curve labelled ‘BLY’ in Fig. 1. The layering instability occurs only in the finite range of g between the red dashed lines; interfaces thus steepen only to a finite value, at which point the instability is arrested.

A reproduction of a numerical solution to the system (3)–(7) with $H = 2000$ is shown in Fig. 2. Figure 2(a) shows the initial development of the layered region, while Fig. 2(b) shows the long-time evolution of the solution. Layers initially start to develop across the interior of the domain, beginning at a distance of ≈ 200 from the top and bottom of the domain. By $t \approx 2 \times 10^4$ (shown red in both panels), a pack of layers of a regular wavelength and amplitude has formed across the full depth of the domain, with the exception of two smooth non-layered regions extending from the top and bottom of the domain to the interior pack of layers. Over time, the layers within the pack undergo sporadic merger events, in which two adjacent interfaces move together and join to form a single interface. At the same time, smooth regions, referred to herein as *edge regions*, expand from the two boundaries of the domain towards the interior at a rate of $z \propto t^{1/2}$, engulfing layers from the outside inwards. Eventually, the edge regions take up the entire domain, meeting in the middle to form a single well-mixed layer across the full depth of the fluid. By totally engulfing the layered region by $t \sim H^2/4$, the development of the edge regions limits investigation into the dynamics of layer mergers beyond this time.

In this paper we develop a BLY-style model and use it to investigate the long-term behaviour of layers in stratified turbulence. We begin by presenting a systematic derivation of a generalised form of the model from the Boussinesq equations, using simple closure assumptions and retaining the parameterisations used by BLY for the dissipation, stirring, and mixing-length. We investigate the predictions of our generalised model, establishing the general effects of viscosity and molecular diffusivity on the conditions for layer formation. Diffusion and viscosity both have a stabilising effect on the system, reducing the range of unstable gradients and the maximum growth rates.

As an inroad towards investigating trends in long-term merger dynamics, we also demonstrate that the adoption of different boundary conditions to those used by BLY can eliminate the expanding edge regions, allowing the long-term dynamics of the layers to be apparent. As noted above, the no-flux conditions of (7) resulted in the development of edge regions that engulf the entire layered region by time $t \sim H^2/4$. We show that the alternative boundary conditions of fixed buoyancy, equivalent to specifying the temperature at the top and bottom of the domain, prevents the expansion of edge regions. The layered region is then changed only by merging behaviour. The removal of the time constraint imposed by the edge regions thus allows us to investigate long-term trends in the dynamics of layer mergers. Each group of mergers approximately halves the number of interfaces, until eventually only a single interface remains. We show that for long times, the number of layers remaining, $N(t)$, is consistent with the scaling $1/N \sim \log t$. An inverse logarithmic dependence of this form has been found previously to arise in solutions to the Cahn-Hilliard (CH) equation for phase separation [27], and an analogy can be made between kinks (separating phases) and interfaces (separating layers of density), allowing the CH equation to be used to model layering (e.g. [28]). BLY demonstrated that the model (3)–(4) can be reduced asymptotically to the CH equation by perturbing the governing equations about the critical point of marginal stability. The logarithmic timescale that we demonstrate here further consolidates and extends this link.

The paper is organised as follows. Section II discusses the derivation of the diffusive model. To begin our analysis of this system, we find uniform steady solutions in Sec. III A. We investigate the linear stability of these steady states in Sec. III B, discussing how the stability is affected by changing the viscosity and molecular diffusivity. In Sec. III C, we consider parameter values relevant to water, where the stratification is due to either a salinity gradient at constant temperature, or a temperature gradient at constant salinity, and compare the differences between these two cases. In Sec. IV we investigate the long-term behaviour of solutions. We begin in Sec. IV A by showing that the adoption of fixed-buoyancy boundary conditions allows layer dynamics to be observed for very long times without the intrusion of edge regions. In Sec. IV B we discuss such long-term numerical solutions of the model in detail, making comparisons with the linear stability predictions described in Sec. III B, and investigating the long-term merger dynamics of the interfaces. We demonstrate that the long-term dynamics of our model are consistent with predictions from Cahn-Hilliard models of layering. Our conclusions and a discussion of possible extensions of the work are contained in Sec. V.

II. MODEL FORMULATION

We consider the evolution of a density-stratified fluid, defined by the velocity $\mathbf{u}(\mathbf{x}, t) = (u, v, w)$ and buoyancy $b(\mathbf{x}, t) = g(\rho_0 - \rho)/\rho_0$, where g is gravitational acceleration, and $\rho(\mathbf{x}, t)$ and ρ_0 are the fluid density and a reference density respectively. The fluid is subject to a body forcing $\Phi(\mathbf{x})$ due to stirring (for example by an oscillating rod or grid) at a speed U and lengthscale d . The dynamics are modelled by the Boussinesq equations:

$$\mathbf{u}_t + \mathbf{u} \cdot \nabla \mathbf{u} = -\frac{1}{\rho_0} \nabla p + b \hat{z} + \nu \nabla^2 \mathbf{u} + \frac{1}{\rho_0} \Phi, \quad (8)$$

$$b_t + \mathbf{u} \cdot \nabla b = \kappa \nabla^2 b, \quad (9)$$

$$\nabla \cdot \mathbf{u} = 0, \quad (10)$$

where ν is the kinematic viscosity and κ the molecular diffusivity. The pressure $p(\mathbf{x}, t)$ represents the perturbation away from the reference hydrostatic pressure $-\rho_0 g z$. We non-dimensionalise the system through the scalings

$$\hat{t} = \frac{U}{d} t, \quad \hat{z} = \frac{1}{d} z, \quad \hat{\mathbf{u}} = \frac{1}{U} \mathbf{u}, \quad \hat{b} = \frac{d}{U^2} b, \quad \hat{p} = \frac{1}{\rho_0 U^2} p, \quad \hat{\Phi} = \frac{d}{\rho_0 U^2} \Phi, \quad (11)$$

where hats denote dimensionless variables. Note that the dimensionless buoyancy gradient $\hat{b}_z = d^2 b_z / U^2$ can be interpreted as a Richardson number, although the velocity used is that of a stirring device, not an imposed shear. On substituting from (11) into equations (8)–(10), and dropping hats, we obtain the non-dimensional Boussinesq equations:

$$\mathbf{u}_t + \mathbf{u} \cdot \nabla \mathbf{u} = -\nabla p + b \hat{z} + \text{Re}^{-1} \nabla^2 \mathbf{u} + \Phi, \quad (12)$$

$$b_t + \mathbf{u} \cdot \nabla b = \text{Pe}^{-1} \nabla^2 b, \quad (13)$$

$$\nabla \cdot \mathbf{u} = 0, \quad (14)$$

where Re is the Reynolds number Ud/ν , and Pe is the Péclet number Ud/κ . Note that the Reynolds and Péclet numbers are related by $\text{Pe} = \text{Pr} \text{Re}$, where $\text{Pr} = \nu/\kappa$ is the Prandtl number. For the purpose of developing our horizontally averaged model, we can assume either impermeability conditions on the sidewalls of the domain, or, for the case of a rectangular cross-section, a horizontally periodic domain.

We now aim to develop, via suitable averaging processes and parameterisations, a model of the form (3)–(4). Oceanic observations of density staircases show that they exhibit little variation over horizontal lengthscales much greater than the thickness of a typical layer [7]. Hence, a horizontally averaged model is an appropriate approximation to gain phenomenological insight, while being significantly easier to solve computationally than the full Boussinesq equations. Our derivation differs from that of BLY, whose equations were derived using scaling arguments alone, with terms parameterised by seeking dimensionally correct combinations of the dependent variables.

Let

$$\langle q \rangle \equiv \frac{1}{A} \int_A q(\mathbf{x}, t) \, dA \quad (15)$$

denote the horizontal spatial average of a quantity $q(\mathbf{x}, t)$ over a horizontal cross-section A at a given height z of the domain; $\langle q \rangle$ is thus a function of z and t . Let $\mathbf{u}_h = (u, v)$ represent the horizontal velocity, and ∇_h the horizontal

gradient operator. The variables will be considered in terms of the sum of their horizontal mean and fluctuation components: $b = \langle b \rangle + b'$, $\mathbf{u}_h = \langle \mathbf{u}_h \rangle + \mathbf{u}'_h$, $w = \langle w \rangle + w'$.

Taking the average of the incompressibility condition (14) and applying either the condition of impermeability or periodicity on the horizontal components of the velocity, we obtain

$$\langle \nabla_h \cdot \mathbf{u}_h \rangle + \langle w_z \rangle = 0, \quad \text{and hence} \quad \langle w \rangle_z = 0. \quad (16)$$

Thus, the horizontally averaged vertical velocity is uniform across the height of the domain. Assuming impermeability conditions on the top and bottom boundaries, it follows that $\langle w \rangle = 0$. Thus there is no mean vertical velocity and $w = w'$.

Our aim is to obtain a model purely in terms of horizontal averages of the buoyancy b and kinetic energy $e = \frac{1}{2} \mathbf{u} \cdot \mathbf{u}$. To this end, we first apply an averaging process to equations (12)–(13), and then parameterise any terms involving products of fluctuations in terms of mean quantities. Taking the horizontal average of (13) and applying (16) gives

$$\langle b \rangle_t + \langle wb' \rangle_z = \text{Pe}^{-1} \langle b \rangle_{zz}. \quad (17)$$

Expression (17) is a diffusion equation for the mean buoyancy $\langle b \rangle$, forced by the eddy flux term $\langle wb' \rangle_z$. The equation for b' is obtained by subtracting the mean equation (17) from the full equation (13) and using a quasilinear approximation to neglect the perturbation-perturbation term $\mathbf{u}'_h \cdot \nabla_h b'$, giving

$$b'_t + w \langle b \rangle_z = \text{Pe}^{-1} \nabla^2 b'. \quad (18)$$

To parameterise the term $\langle wb' \rangle$ in (17) in terms of mean quantities, we use a scaling argument to represent the derivatives algebraically. We assume that the mean of the square of the vertical velocity is a constant multiple of the mean total kinetic energy $\langle e \rangle = \langle \mathbf{u} \cdot \mathbf{u} \rangle / 2$, i.e.

$$\langle w^2 \rangle = \beta^2 \langle \mathbf{u} \cdot \mathbf{u} \rangle / 2 = \beta^2 \langle e \rangle, \quad (19)$$

for some dimensionless constant β . We assume that the turbulence varies on a mixing lengthscale l (to be parameterised as a function of the dependent variables) and on the dynamical timescale $\tau \sim l / \beta \langle e \rangle^{1/2}$, defined as the characteristic time to move a distance l vertically. These length and time scales are designed to provide approximations of the characteristic values for the derivatives $\partial_t \sim 1/\tau = \beta \langle e \rangle^{1/2} / l$ and $\nabla^2 \sim -1/l^2$. Multiplying the fluctuation equation (18) by w , averaging and rearranging gives the turbulent buoyancy flux as

$$\langle wb' \rangle = - \frac{l^2 \langle w^2 \rangle}{\beta l \langle e \rangle^{1/2} + \text{Pe}^{-1}} \langle b \rangle_z. \quad (20)$$

Using (19), this flux can be written in terms of $\langle b \rangle$ and $\langle e \rangle$ as

$$\langle wb' \rangle = -\beta \frac{l^2 \langle e \rangle}{l \langle e \rangle^{1/2} + (\beta \text{Pe}^{-1})} \langle b \rangle_z. \quad (21)$$

Finally, combining (17) and (21) gives the equation for the averaged buoyancy:

$$\frac{1}{\beta} \langle b \rangle_t = \left(\frac{l^2 \langle e \rangle}{l \langle e \rangle^{1/2} + (\beta \text{Pe}^{-1})} \langle b \rangle_z \right)_z + (\beta \text{Pe})^{-1} \langle b \rangle_{zz}. \quad (22)$$

The first term on the right hand side of (22) represents the turbulent transport of $\langle b \rangle$, and the second term molecular diffusion. We note that incorporating molecular diffusion has not only introduced the $(\beta \text{Pe})^{-1} \langle b \rangle_{zz}$ term, but also altered the form of the turbulent flux so that it now also depends on Pe^{-1} . To complete the model, we must couple equation (22) with an evolution equation for the horizontally averaged kinetic energy $\langle e \rangle$, and provide a parameterisation for the mixing length l .

We formulate the energy equation by taking the scalar product of the momentum equation (12) with \mathbf{u} , giving

$$e_t + \nabla \cdot (\mathbf{u}e) = \nabla \cdot (\mathbf{u}p) + wb + \text{Re}^{-1} (\nabla^2 e - |\nabla \mathbf{u}|^2) + \mathbf{u} \cdot \Phi. \quad (23)$$

The terms on the right hand side of (23) represent, in order, the effect of pressure, the conversion from potential to kinetic energy, diffusion of kinetic energy, viscous dissipation $D = -\text{Re}^{-1} |\nabla \mathbf{u}|^2$ and production through stirring $P = \mathbf{u} \cdot \Phi$. Taking the horizontal average of (23) gives

$$\langle e \rangle_t + \langle we' \rangle_z - \text{Re}^{-1} \langle e \rangle_{zz} = \langle wb' \rangle - \langle D \rangle + \langle P \rangle. \quad (24)$$

The fluctuation turbulent energy flux $\langle we' \rangle$ can be parameterised in a similar way to the buoyancy flux: we subtract (24) from (23) to obtain an equation for the fluctuation energy, approximate the derivatives, then multiply by $w/2$ and take the average as in (21) to parameterise the fluctuation flux $\langle we' \rangle$. This leads to the following equation for the averaged energy:

$$\frac{1}{\beta} \langle e \rangle_t = \left(\frac{l^2 \langle e \rangle}{l \langle e \rangle^{1/2} + (\beta \text{Re})^{-1} \langle e \rangle_z} \right)_z - \frac{l^2 \langle e \rangle}{l \langle e \rangle^{1/2} + (\beta \text{Pe})^{-1} \langle b \rangle_z} + (\beta \text{Re})^{-1} \langle e \rangle_{zz} - \frac{1}{\beta} \langle D \rangle + \frac{1}{\beta} \langle P \rangle. \quad (25)$$

In an exactly analogous manner to the derivation of the buoyancy equation (22), the inclusion of viscosity and molecular diffusion has altered the energy flux and potential energy transfer terms, as well as introducing a standard viscous diffusion term.

To close the system, a parameterisation is required for the turbulent lengthscale l in terms of the dependent variables $\langle b \rangle$ and $\langle e \rangle$. Following BLY, we adopt a lengthscale of the form (6), but it should be noted that this is not the only possible parameterisation for the lengthscale. We anticipate that any monotonic function that interpolates between the stirring length when the stratification is weak, and a smaller length when the stratification is strong, would serve the same purpose. We choose here to adopt the BLY lengthscale in the form (6) as it allows us to compare the results of our model directly with those of BLY, so that our study of the effects of diffusion and different boundary conditions is not affected by the further complication of adopting a different mixing length.

To parameterise the dissipation $\langle D \rangle$ and source $\langle P \rangle$, we also follow BLY. For the dissipation, the only combination of e and l that provides the correct dimensions for D is $D = \varepsilon e^{3/2}/l$, where ε is a dimensionless number that we treat as a parameter. This parameterisation of dissipation is commonly used in k - ε models of turbulence (e.g. [29]). The parameterisation for the source term P is less obvious, but we use BLY's ‘equipartition’ form for energy production, which is formulated such that the eddy speed $e^{1/2}$ adjusts to the velocity scale of the stirring device on the eddy turnover timescale $l/e^{1/2}$, and which provides an N-shaped flux-gradient relation. The dimensionless parameter β in equations (22) and (25) acts simply as a scale factor on the time derivative, effectively setting a new dimensionless time variable $\tilde{t} = \beta t$, with new dimensionless parameters defined similarly: $\tilde{\text{Pe}} = \beta \text{Pe}$, $\tilde{\text{Re}} = \beta \text{Re}$ and $\tilde{\varepsilon} = \beta \varepsilon$. With these rescalings, all factors of β disappear from (22) and (25), including in the parameterisations for the terms $\langle D \rangle/\beta$ and $\langle P \rangle/\beta$.

By adopting these rescaled forms of time and the dimensionless parameters, and dropping tildes and angled brackets from (22) and (25), we obtain the full model as

$$b_t = \left(\frac{l^2 e}{l e^{1/2} + \text{Pe}^{-1} b_z} \right)_z + \text{Pe}^{-1} b_{zz}, \quad (26)$$

$$e_t = \left(\frac{l^2 e}{l e^{1/2} + \text{Re}^{-1} e_z} \right)_z - \frac{l^2 e}{l e^{1/2} + \text{Pe}^{-1} b_z} + \text{Re}^{-1} e_{zz} - \varepsilon (e - 1) \frac{e^{1/2}}{l}, \quad (27)$$

$$l = l(b_z, e) = \frac{e^{1/2}}{(e + b_z)^{1/2}}. \quad (28)$$

The system (26)–(28) forms a coupled nonlinear diffusion model describing the evolution of the horizontally averaged buoyancy $b(z, t)$ and energy density $e(z, t)$, dependent on turbulent fluxes parameterised using a mixing length $l(b_z, e)$. The second term in the energy equation (27) is necessarily the same as the turbulent buoyancy flux, and accounts for transfer between potential and kinetic energy. The final term in (27) represents the combined effects of viscous dissipation and the energy source from stirring. When $e = 1$, dissipation balances production. If $e < 1$, there is a net source of energy; if $e > 1$, there is a net sink. The BLY model can be recovered from the system (26)–(28) by setting $\text{Pe}^{-1} = \text{Re}^{-1} = 0$, which turns off both viscous and molecular diffusion.

III. CONDITIONS FOR INITIAL LAYER DEVELOPMENT

In this section, we consider the initial development of layers, and investigate the effects of viscosity and diffusion on the system through varying the inverse Reynolds number Re^{-1} and inverse Péclet number Pe^{-1} . We saw in Sec. II that these parameters appear not only as standard diffusion terms, but also in the flux terms in equations (26)–(27).

We begin, in Sec. III A, by seeking steady solutions that have uniform b_z and e . We then proceed to analyse their linear stability in Sec. III B, finding that larger values of Pe^{-1} and Re^{-1} both suppress the instability. In Sec. III C, we consider the combined effects of changing Pe^{-1} and Re^{-1} together, using values relevant for water, with the stratification provided either by a salinity gradient at constant temperature, or a temperature gradient at constant salinity.

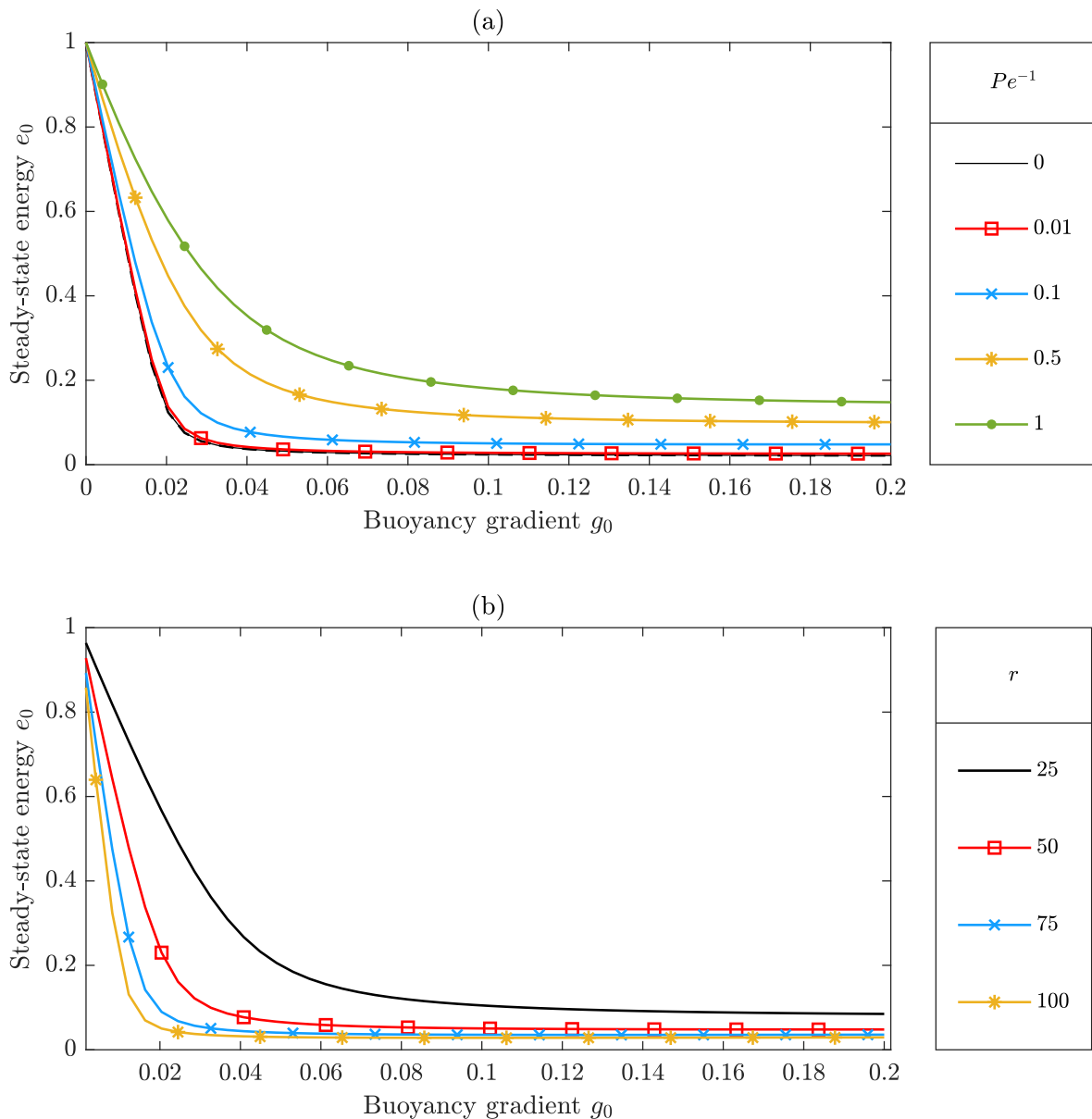


FIG. 3. Steady-state energy plotted against buoyancy gradient. In (a), $r = 50$ is fixed and Pe^{-1} varies; in (b), $Pe^{-1} = 0.1$ is fixed and r varies.

A. Uniform-gradient steady states

To begin our linear stability analysis, we return to the full system (26)–(28), and seek uniform steady states $b = g_0 z$, $e = e_0$, where g_0 and e_0 are constants. For such basic states, the buoyancy equation (26) is trivially satisfied, and the energy equation (27) becomes

$$0 = -\frac{l^2 e_0}{l e_0^{1/2} + Pe^{-1}} g_0 - \varepsilon \frac{e_0^{1/2}}{l} (e_0 - 1). \quad (29)$$

On substituting for l from (28) and rearranging, we obtain the steady energy equation

$$r e_0^2 g_0 + (e_0 - 1)(e_0 + g_0)e_0 + Pe^{-1}(e_0 - 1)(e_0 + g_0)^{3/2}. \quad (30)$$

Figure 3 shows the exact solutions to (30) as solid lines, for a range of values of Pe^{-1} and r . In Fig. 3(a) we fix $r = 50$ while varying Pe^{-1} . In every case, $e_0 = 1$ at $g_0 = 0$, corresponding to a dimensional energy of $U^2/2$ — the

energy is set by the stirring speed. As g_0 increases, the energy decreases monotonically. For small values of Pe^{-1} , the solutions are similar to the BLY solution (shown black), but for larger Pe^{-1} the profile is significantly shallower, with $e_0(g_0)$ decreasing more gradually.

Figure 3(b) also shows the steady state energy $e_0(g_0)$, this time fixing $\text{Pe}^{-1} = 0.1$ while varying r . Here we see that larger values of r produce profiles where $e_0(g_0)$ decreases more steeply. For large values of r (small ε), the combined viscous dissipation and stirring term $\varepsilon e_0^{1/2}(e_0 - 1)/l$ in the steady state equation (29) is $O(\varepsilon)$. For the equation to be satisfied, the buoyancy flux term $-l^2 e_0 g_0 / (l e_0^{1/2} + \text{Pe}^{-1})$ must therefore also be small. This requires either e_0 or g_0 to be sufficiently small, producing the sharp decrease in $e_0(g_0)$ shown in the figure.

B. Stability and conditions for layering

We now proceed to investigate the linear stability of the uniform-gradient steady states found in Sec. III A. To do this, we will consider results derived by BLY for a more general system, and show how they apply to our model. The system (26)–(27) can be written in the form

$$g_t = f_{zz}, \quad (31)$$

$$e_t = (\kappa e_z)_z + p, \quad (32)$$

where the functions $f(g, e)$, $p(g, e)$ and $\kappa(g, e)$ are defined as

$$f = \left(\frac{l^2 e}{l e^{1/2} + \text{Pe}^{-1}} + \text{Pe}^{-1} \right) g, \quad (33)$$

$$p = -\frac{l^2 e}{l e^{1/2} + \text{Pe}^{-1}} g - \varepsilon \frac{e^{3/2}}{l} + \varepsilon \frac{e^{1/2}}{l}, \quad (34)$$

$$\kappa = \frac{l^2 e}{l e^{1/2} + \text{Re}^{-1}}. \quad (35)$$

BLY presented a linear stability analysis of the general system (31)–(32), which can be applied for any given specification of $f(g, e)$, $p(g, e)$ and $\kappa(g, e)$. Considering the more general form (31)–(32) thus allows us to apply the linear stability results obtained by BLY to our generalised situation allowing for viscosity and molecular diffusion, as given by (33)–(35). The general form also means that the results remain valid if we change any parameterisations in the system, such as presenting a different formulation of the mixing length l .

BLY showed that the steady state $g = g_0$, $e = e_0$, is linearly unstable if

$$F'(g_0) := \frac{f_g p_e - f_e p_g}{p_e} < 0, \quad (36)$$

where the partial derivatives $f_g(g, e)$, $f_e(g, e)$, $p_g(g, e)$, $p_e(g, e)$ are evaluated in the steady state (g_0, e_0) , and $F'(g_0)$ is defined as the total derivative of f with respect to g , evaluated at $(g_0, e_0(g_0))$. In essence, this represents the Phillips effect (cf. condition (2)), but generalised to a more complex, physically-derived diffusion problem. BLY further proposed that, in order for layering to occur, the flux-gradient relation $F'(g)$ should be N-shaped, so that there is instability only for an intermediate range of g , with very low and very high gradients being stable.

The system (31)–(32) contains two time derivatives, so the linear stability analysis produces two growth rates. The first is positive if condition (36) is satisfied. The second, ‘energy mode’, growth rate is equal to p_e , and allows for the possibility of an instability arising from the energy equation (32) alone, without any interaction with the buoyancy equation. This could happen if the forcing were too strong, or the buoyancy gradient were negative, for example. For the model to be an accurate representation of the layering mechanism, it is necessary that the only instability comes from the Phillips effect. Hence the energy mode must be stable, so we require $p_e < 0$.

For the functions relevant to our model (33)–(35), the condition $p_e < 0$ is satisfied for all values of (g_0, e_0) , Pe^{-1} and Re^{-1} . Hence the energy mode is damped, with the only instability arising from the Phillips effect. Note that the inverse Péclet number Pe^{-1} affects f and p , while the inverse Reynolds number Re^{-1} is contained only in κ . Because the condition for instability (36) depends only on f and p , this means that varying Re^{-1} independently of Pe^{-1} does not change whether or not the system is unstable, but only affects the range of unstable wavenumbers.

Figure 4(a) shows flux-gradient relations $f(g)$ for a range of values of Pe^{-1} , for the illustrative case $r = 50$. The plots display the clear N-shape required for the layering instability for values of $\text{Pe}^{-1} < 0.113$ (a critical value that depends on r). As Pe^{-1} increases, the N-shape flattens. For all $\text{Pe}^{-1} > 0.113$, $f(g)$ is a monotonically increasing function.

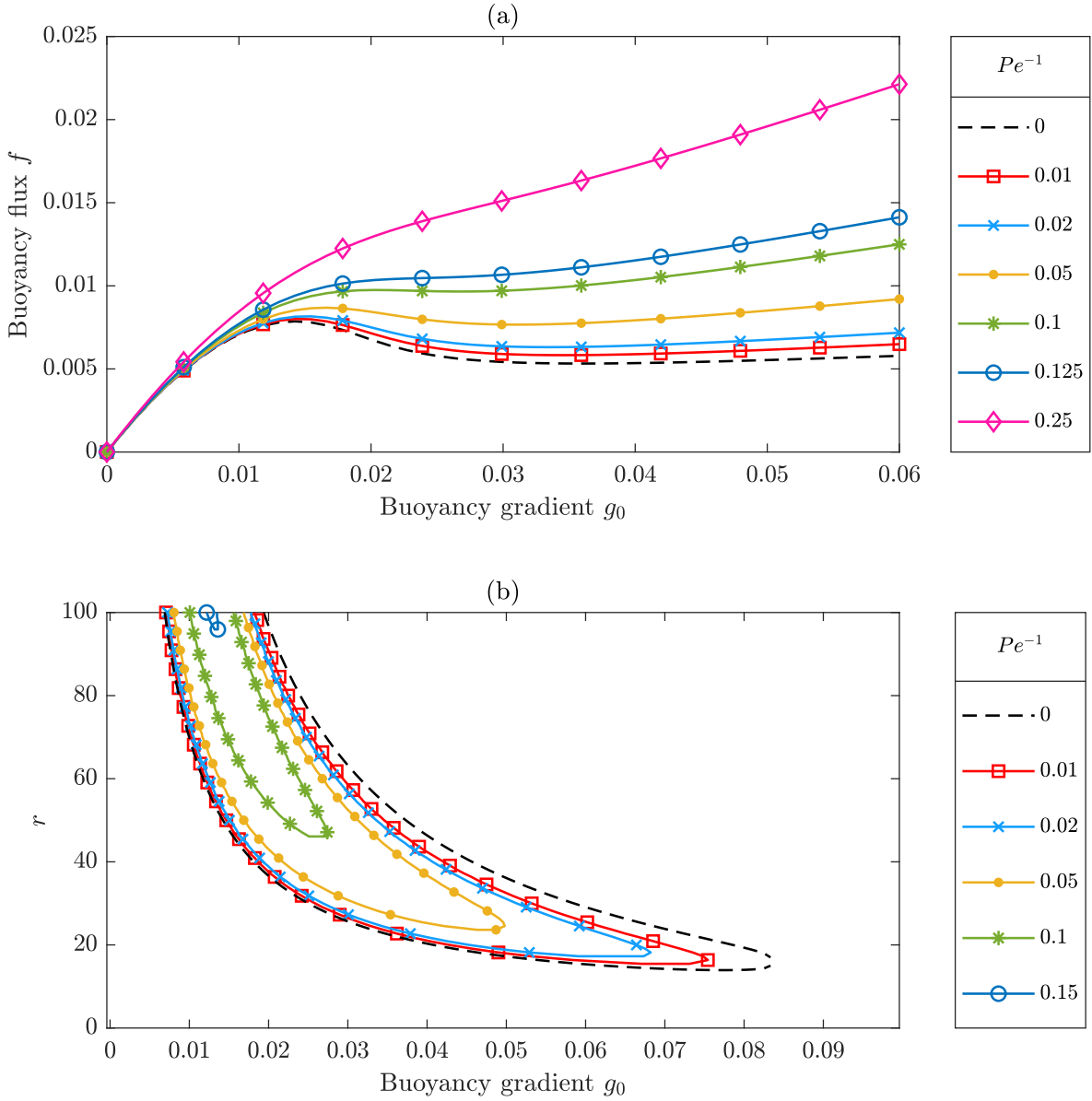


FIG. 4. (a) Flux-gradient relations for a selection of values of Pe^{-1} , for $r = 50$, calculated by substituting the steady-state energy e_0 (found as exact solutions of (30)) into the buoyancy flux $f(g, e)$ given by (33). The N-shape curve required for the layering instability is displayed by the smaller values of Pe^{-1} . (b) Loci of $F'(g_0; r) = 0$, for a range of Pe^{-1} . For each value of r , the gradients g_0 inside the curve are unstable.

Thus, with all other conditions identical, a sufficiently high density diffusion (sufficiently large Pe^{-1}) eventually suppresses the layering instability.

Figure 4(b) shows the loci on which $F'(g_0; r) = 0$ for a range of values of Pe^{-1} . These lines correspond to the top of the peak and bottom of the trough of the N-shape in Fig. 4(a). It is clear that for any value of r , the unstable range of g_0 is greatest when $Pe^{-1} = 0$. As Pe^{-1} increases, the unstable range of g_0 at fixed r decreases, and the critical value of r above which instability occurs increases. The loci in Fig. 4(b) illustrate that when the stratification is too weak, no layering is possible — physically it seems reasonable that without a strong enough gradient, mixing will simply destroy the stratification and lead to homogeneous turbulence. On the other hand, when the gradient is too large, the stratification cannot be sufficiently disturbed by the mixing, so no layers form. Using the expressions for f and p given by (33)–(34), we find that the outermost (black, $Pe^{-1} = 0$) locus is represented by

$$r(g_0) = \frac{4 - 3g_0 \pm 2\sqrt{1 - 12g_0}}{3g_0}. \quad (37)$$

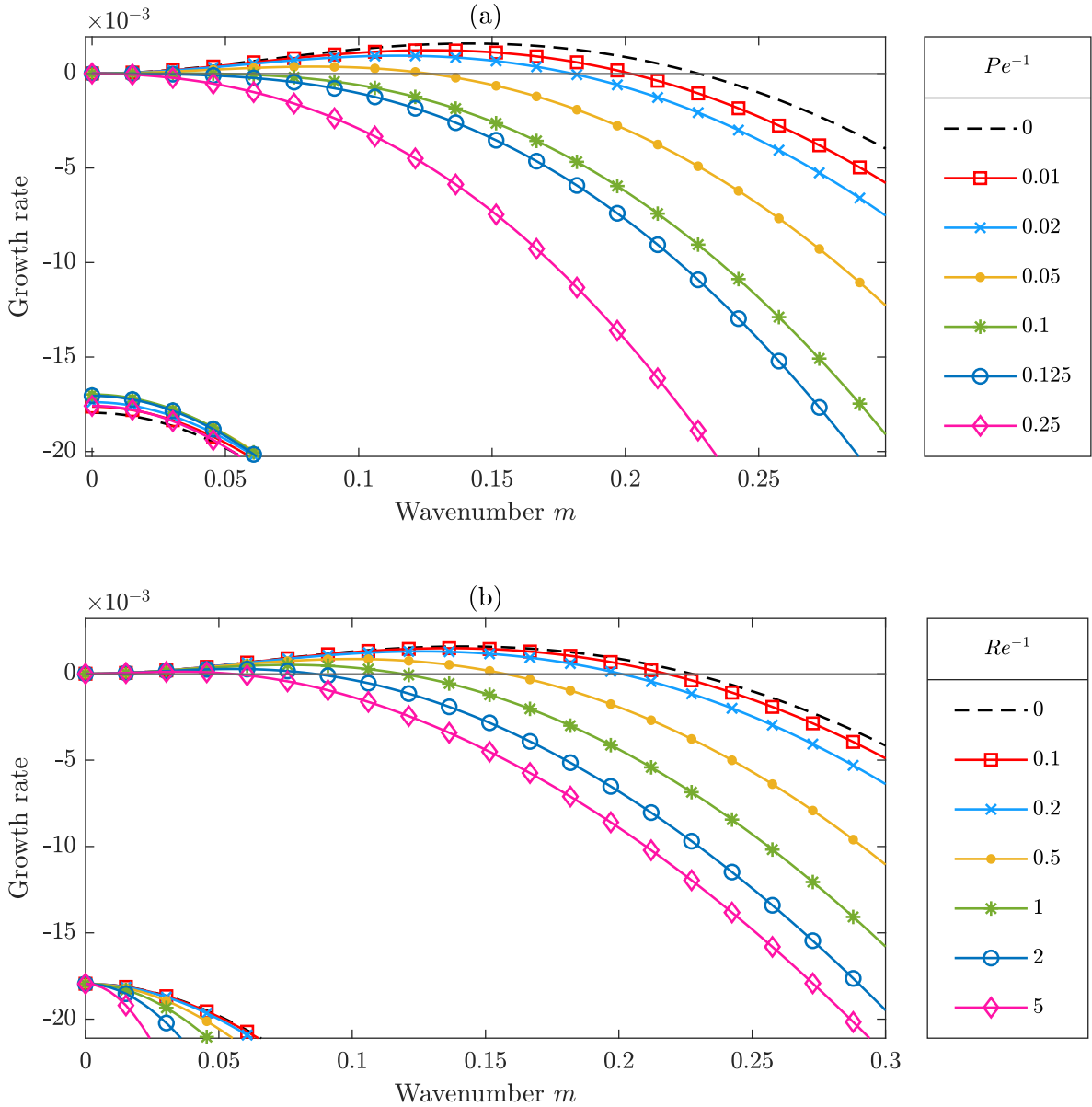


FIG. 5. Growth rate plotted as a function of wavenumber, for $r = 50$ and $g_0 = 0.0218$. In (a), $Re^{-1} = 0$ is fixed and Pe^{-1} varies; in (b), $Pe^{-1} = 0$ is fixed and Re^{-1} varies. Since the parameters are linked by $Pe = Pr Re$, (a) corresponds to the limit of $Pr = 0$, and (b) to $Pr \rightarrow \infty$. The dashed black curve represents the diffusionless system. The lower set of curves represents the damped energy mode.

The case with the $-$ sign represents the left hand part of the locus; the $+$ sign represents the right hand part. The tip of the locus is at $g_0 = 1/12$, where both expressions are equal. Across all values of r and Pe^{-1} , this is the maximum possible gradient for layering. For $r \rightarrow 0$, expression (37) reduces to the two asymptotes

$$g_1(r) \sim \frac{2}{3r}, \quad g_2(r) \sim \frac{2}{r}. \quad (38)$$

Thus, for any finite value of r , there is a positive range of g_0 for which the stratification is too weak for layering, as well as a finite range of g_0 for which layering is possible. We can see from Fig. 4 that increasing the value of Pe^{-1} shrinks the locus of marginal stability, both by increasing the critical value of r for instability (i.e. the tip of the curve), and by decreasing the unstable range of g_0 for each value of r .

The plots in Fig. 5 show how the growth rate of perturbations depends on the wavenumber. In panel (a), $Re^{-1} = 0$ is fixed and Pe^{-1} varies, while panel (b) has $Pe^{-1} = 0$ while Re^{-1} varies. The parameters are linked by the relation

Temperature/ $^{\circ}\text{C}$	Salinity/ ‰	Pr	Sc
0	0	13.18	1620
0	20	13.22	1680
0	40	13.34	1750
10	0	9.32	831
10	20	9.39	884
10	40	9.52	934
20	0	6.95	480
20	20	7.04	514
20	40	7.17	547

TABLE I. Prandtl and Schmidt numbers of water at various temperatures (in degrees Celsius) and salinities (in parts per thousand). The values of Pr are taken from [30, 31] and those of Sc from [32].

$\text{Pe} = \text{Pr Re}$, so panel (a) shows the limit of $\text{Pr} = 0$, panel (b) the limit of $\text{Pr} \rightarrow \infty$. In both cases, there is one set of unstable modes, as well as a second stable set of growth rates representing the energy mode. We see that, in accordance with the stability criteria discussed in Sec. III B, higher values of Pe^{-1} suppress the instability entirely. Furthermore, increasing Re^{-1} has no effect on the criterion for instability, but alters the range of unstable wavenumbers.

To summarise, the introduction of either molecular diffusivity or viscosity suppresses the layering instability. Viscosity does not change whether or not a steady state is unstable, but reduces the unstable range of wavenumbers and, consequently, the wavenumber of maximum growth rate. Hence, we expect larger values of Re^{-1} to produce staircases with thicker layers and fewer interfaces. Incorporating molecular diffusivity has the same effect of decreasing the unstable range of wavenumbers, but can also suppress the instability entirely by reducing the unstable range of buoyancy gradients. We conclude that introducing diffusion to the system will make staircases less pronounced, by increasing the gradient in layers, and decreasing the gradient in interfaces.

C. Implications for typical values of Pe^{-1} and Re^{-1}

To examine simultaneously the combined effects of viscosity and diffusion, we consider some realistic parameters for both temperature- and salt-stratified water. Here, temperature-/salt-stratified means that the density gradient is caused by a variation in temperature/salt alone. Note that for a temperature-stratified fluid,

$$\text{Pe} = \text{Pr Re}, \quad (39)$$

where $\text{Pr} = \nu/\kappa$ is the Prandtl number. For a salt-stratified fluid with solutal diffusivity κ_S , the analogue of Pr is the Schmidt number $\text{Sc} = \nu/\kappa_S$. Some characteristic values of Pr and Sc are shown in Table I, for typical conditions relevant to both oceanic and laboratory settings. For a reasonable range of temperatures and salinities, $\text{Pr} \sim 10$, while $\text{Sc} \sim 100\text{-}1000$. Hence, for a given Reynolds number, the Péclet number is 10-100 times smaller for salt-stratified water than for the temperature-stratified case. For the ranges shown in Table I, variations in salinity have only a small effect on Pr and Sc compared to variations in temperature. In a typical turbulent terrestrial flow, $\text{Re} \gtrsim O(1000)$, but Fig. 5 shows that even for $\text{Re}^{-1} = 0.1$, the growth rate profile is very close to that for $\text{Re}^{-1} = 0$. As such, to demonstrate fully the effect of parameter choices we will consider a range of larger values of Re^{-1} .

Figure 6 shows plots of growth rate versus wavenumber for three values of Re^{-1} and for a range of values of Pr and Sc; the Péclet number follows from the relations $\text{Pe}^{-1} = (\text{Pr Re})^{-1}$ and $\text{Pe}^{-1} = (\text{Sc Re})^{-1}$. In Fig. 6(a), we take values relevant for temperature-stratified water. Instability occurs only for sufficiently small Re^{-1} ; all the solutions for $\text{Re}^{-1} = 10$ are stable. Larger values of Pr increase both the range of unstable g_0 and the maximum growth rate, as they give smaller values of Pe^{-1} . For the case of $\text{Re}^{-1} = 1$, the system is unstable only for the higher values of Pr chosen. In Fig. 6(b), parameter values are taken to be relevant for salt-stratified water; here, all the values considered lead to instability. There is little difference between the results for the four different Schmidt numbers, but increasing Re^{-1} does decrease the range of unstable g_0 and the maximum growth rates. This is because the Schmidt numbers are large and hence the inverse Péclet numbers are small; e.g. for $\text{Re}^{-1} = 0.1$, the values of Sc used correspond to $\text{Pe}^{-1} = O(10^{-4})$. In contrast, the values of Pr used in the temperature-stratified case correspond to $\text{Pe}^{-1} = O(10^{-2})$. Hence, changing the background temperature, and therefore Pr, has a much greater effect on Pe^{-1} in the temperature-stratified case than changing Sc in a salt stratification. The existence of the layering instability is therefore more sensitive to the background temperature, and requires larger Reynolds numbers, in a temperature-stratified fluid than in a salt-stratified fluid.

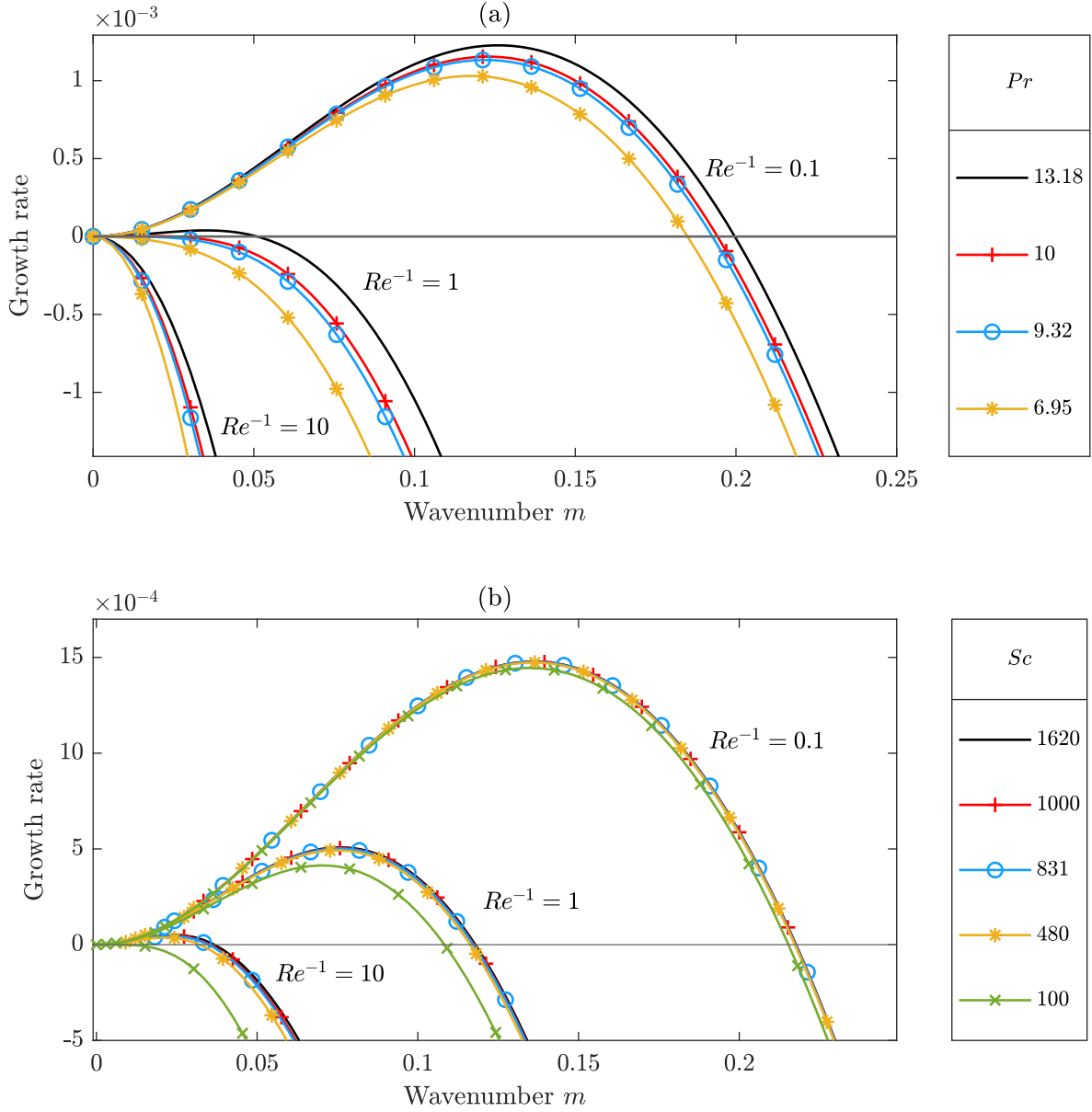


FIG. 6. Growth rate plotted as a function of wavenumber, for (a) temperature- and (b) salt-stratified fluids, for $r = 50$, $g_i = 0.0218$, with three different choices of Re^{-1} and a range of values of Prandtl and Schmidt numbers. The values of Pr and Sc are chosen to be representative of water under common terrestrial conditions, as seen in Table I. For comparison with Fig. 5, note that in (a), $Pe^{-1} = (Pr Re)^{-1}$, and in (b), $Pe^{-1} = (Sc Re)^{-1}$.

Table II shows maximum growth rates and their corresponding wavenumbers, for characteristic values of Pr and Sc in oceanic configurations, as well as for two smaller choices of Pr . There is only a very slight difference between the results for $Pr = 1$ and $Pr = 0$, so a more detailed study of the small Pr region of parameter space is unlikely to reveal any new behaviour. From Table II and Figs. 4-6, we see that increasing density diffusion decreases the area in (g_0, r) parameter space that is unstable. Increasing density diffusion or viscosity decreases the range of unstable wavenumbers for each background gradient, as well as decreasing the wavenumber of maximum growth rate and the maximum growth rate itself.

	Re^{-1}	Pe^{-1}	m_{\max}	$n = Hm/2\pi$	$L = 2\pi/m$	growth rate
BLY case	0	0	0.14	45	44	1.6×10^{-3}
Pr = 10	0.1	0.01	0.12	40	51	1.1×10^{-3}
Pr = 10	1	0.1	0.018	5.8	350	2.6×10^{-6}
Pr = 10	10	1	no unstable wavenumbers			
Sc = 1000	0.1	10^{-4}	0.14	43	46	1.5×10^{-3}
Sc = 1000	1	10^{-3}	0.076	24	83	5.0×10^{-4}
Sc = 1000	10	10^{-2}	0.024	7.7	26	4.7×10^{-5}
Pr = 1	0.001	0.01	0.13	41	48	1.2×10^{-3}
Pr = 1	0.01	0.1	0.027	8.6	230	6.6×10^{-6}
Pr = 1	0.1	1	no unstable wavenumbers			
Pr = 0	0	0.01	0.13	41	48	1.2×10^{-3}
Pr = 0	0	0.1	0.027	8.6	230	6.9×10^{-6}
Pr = 0	0	1	no unstable wavenumbers			

TABLE II. Predicted dimensionless wavenumbers of the mode of maximum growth rate m_{\max} , and the corresponding dimensionless growth rates, for characteristic values of Pr, Sc and Re^{-1} , with $r = 50$, $g_0 = 0.0218$. For $Pr \lesssim 1$, there is little difference from the $Pr = 0$ case. Plots of wavenumber versus growth rate are shown for selected parameter choices in Fig. 6.

IV. LONG-TERM EVOLUTION OF LAYERED SOLUTIONS

In this section, we present solutions to the model (26)–(28), focusing on the long-term dynamics. In Sec. IV A, we demonstrate that by adopting fixed-buoyancy boundary conditions, the expanding edge regions that appear in solutions to the BLY model (3)–(7) are avoided, allowing the observation of layer dynamics to long times. An investigation of the long-term dynamics is presented in Sec. IV B, where we show how the predictions of Sec. III C are manifest in the solutions at long times. Furthermore, we demonstrate a general trend for the long-term behaviour.

A. The effects of fixed-buoyancy boundary conditions on the long-term behaviour

We begin by investigating the effects of fixed-buoyancy boundary conditions on the system. For simplicity, and to isolate the effects of the boundary conditions, we take $Pe^{-1} = Re^{-1} = 0$ in this section, reducing the model (26)–(27) to the BLY system (3)–(4) exactly. Once the effects of the boundary conditions are understood, we will reincorporate finite molecular diffusivity and viscosity.

The no-flux boundary conditions (7) ensure that the total energy is changed only by dissipation and stirring. For a temperature-stratified fluid, this is equivalent to the upper and lower boundaries being insulated and impermeable. The no-flux conditions admit an approximate similarity solution describing the growth of the edge region towards the centre of the domain, represented by $b_z = g(z/t^{1/2})$, $e = e(z/t^{1/2})$. This prediction was confirmed numerically by BLY, who demonstrated that the edge regions expand into the interior at a rate of $z \sim t^{1/2}$. For such a similarity solution to exist, it is necessary that boundary conditions are imposed on the buoyancy gradient $g = b_z$, rather than on the buoyancy itself, b . Hence it is of interest to determine how the edge regions behave, and indeed if they even exist, if different boundary conditions are imposed.

In the case of a temperature-stratified fluid, a common experimental setup is a fluid layer between two conducting plates held at constant temperatures. For a statically stable gradient, we consider a hot plate above a cold plate, and adopt the Dirichlet conditions

$$b(0, t) = 0, \quad b(H, t) = g_0 H, \quad (40)$$

forming a uniform stable stratification. Here, g_0 is the initial uniform background buoyancy gradient, and H is the fluid depth. Without loss of generality, the buoyancy on the bottom boundary can be taken as zero, as the equations depend only on buoyancy gradients. In contrast to the choice of no-flux boundary conditions, the fixed-buoyancy condition (40) allows us to take a uniform background buoyancy gradient $g(z) = g_0$, which we use as a basic state for the system, creating a uniform stratification. Taking this solution to be a steady basic state gives $e(z) = e_0(g_0)$, uniform throughout the domain. Thus a no-flux (Neumann) condition on the energy is possible:

$$e_z(0) = e_z(H) = 0. \quad (41)$$

Alternatively, we can choose to fix the energy on the boundaries with the Dirichlet condition

$$e(0, t) = e(H, t) = e_0. \quad (42)$$

In considering appropriate initial conditions, we begin by noting that (40) admits steady-state solutions with both b_z and e uniform with height, for either choice of condition on the energy, (41) or (42). Assuming that $b = g_0 z$ and $e = e_B$, we find steady solutions to (26)–(28) by setting time derivatives to zero. Taking a uniform buoyancy gradient and uniform energy means that all the spatial derivatives also vanish, leaving a quadratic equation for $e_B(g_0)$, with solution

$$e_B(g_0) = \frac{1}{2} \left(1 - g_0(1+r) + \sqrt{(1 - g_0(1+r))^2 + 4g_0} \right), \quad (43)$$

where $r = 1/\varepsilon$ [20]. For the case of no stratification ($g_0 = 0$), the steady-state energy $e_B = 1$ is associated with the non-dimensional stirring lengthscale. As $g_0 \rightarrow \infty$, $e_B \rightarrow 0$, thereby demonstrating the damping of motion as the stratification is increased.

For the buoyancy initial condition, we take a uniform gradient steady state plus a sinusoidal perturbation of amplitude a and wavenumber $2\pi n/H$:

$$b(z, 0) = g_0 \left[z - a \sin \left(\frac{2\pi n z}{H} \right) \right], \quad (44)$$

$$e(z, 0) = e_B(g_0), \quad (45)$$

where $e_B(g_0)$ is given by (43). We set the amplitude to be $a = 0.001$. The integer n is chosen to produce the maximum linear growth rate for perturbations about this steady state (cf. Sec. III B), ensuring that layers develop quickly from the perturbations, with little interference from other wavenumbers. BLY used the parameter values $g_0 = 0.0218$, $r = 50$, $H = 2000$, and demonstrated that, for these values, the dominant wavenumber corresponds to $n = 45$. To facilitate comparison with BLY's results, we will adopt the same values.

All the numerical solutions of the full nonlinear system were obtained using the MATLAB `pdepe` solver. Figure 7 shows the short- and long-time evolution of solutions to equations (26)–(28). All plots have 4000 spatial mesh points. The early evolution plots have 1000 time steps, while long-time solutions were calculated using a series of nine integrations, each with 1000 time steps. There are 1000 linearly spaced time steps between each time labelled on the vertical axis, giving a piecewise linear time axis, with the size of a time step increasing by a factor of 10 or 100 between each label. The solutions are not sensitive to finer spatial resolutions or integration tolerances, and the `pdepe` solver chooses timesteps dynamically to ensure that the solutions are well resolved in time.

Figures 7(a,b) show the integration carried out with no-flux (Neumann) boundary conditions on the energy (41). The initial perturbation grows into a regular pattern of spikes in the buoyancy gradient $g(z, t)$, separating regions in which the fluid is well mixed and the gradient is small. The spikes represent smeared interfaces separating the well-mixed layers. At this stage, the evolution is similar to that arising from the no-flux buoyancy boundary conditions (7) (cf. Fig. 2). A key difference, however, is that the region in which layers form extends across the full depth of the domain, with little influence from the boundaries (an aspect that becomes increasingly important at later times). Initially we see 45 spikes (layer interfaces) in the buoyancy gradient profile $g(z, t)$. The wavenumber of this initial pattern of layering matches that of the initial perturbation $m = 45(2\pi/H)$. The interfaces begin to merge at $t \approx 1.6 \times 10^5$, with mergers happening evenly across the domain. After the first merger, the spike height (i.e. the maximum gradient in an interface) is approximately double that of the initial spikes. After subsequent mergers take place, the height of the spikes remains constant, with successive mergers doubling the width of each spike, as the maximum unstable gradient has been reached. The state at $t \approx 1 \times 10^{16}$ is not the final state of the system — the solution will continue to evolve through mergers until eventually a single interface remains.

Figures 7(c,d) show the integration carried out with fixed-energy (Dirichlet) boundary conditions (42) instead of no-flux (Neumann) conditions (41), with all other parameters and conditions identical to those used in the simulation shown in Figs. 7(a,b). As with the Neumann conditions, the initial perturbation develops into 45 spikes, which undergo mergers. However, the first mergers now appear at the earlier time of $t \approx 15000$, first near the boundaries, and progress inwards towards the centre of the domain, until all but one spike has merged with its neighbours by $t \approx 110000$. After the initial development of the layers, the outermost interfaces move to the boundaries, resulting in a thicker layer. This thicker layer provokes the second spike from the boundary to merge with the third, creating another thicker layer. In turn this provokes a merger of the next two spikes, with the process continuing into the interior. After this first group of mergers, the dynamics are very similar to those in Figs. 7(a,b). Successive mergers take place evenly across the domain, and the most notable difference from Figs. 7(a,b) is the time at which mergers happen — which is a consequence of the different times at which the first mergers are complete.

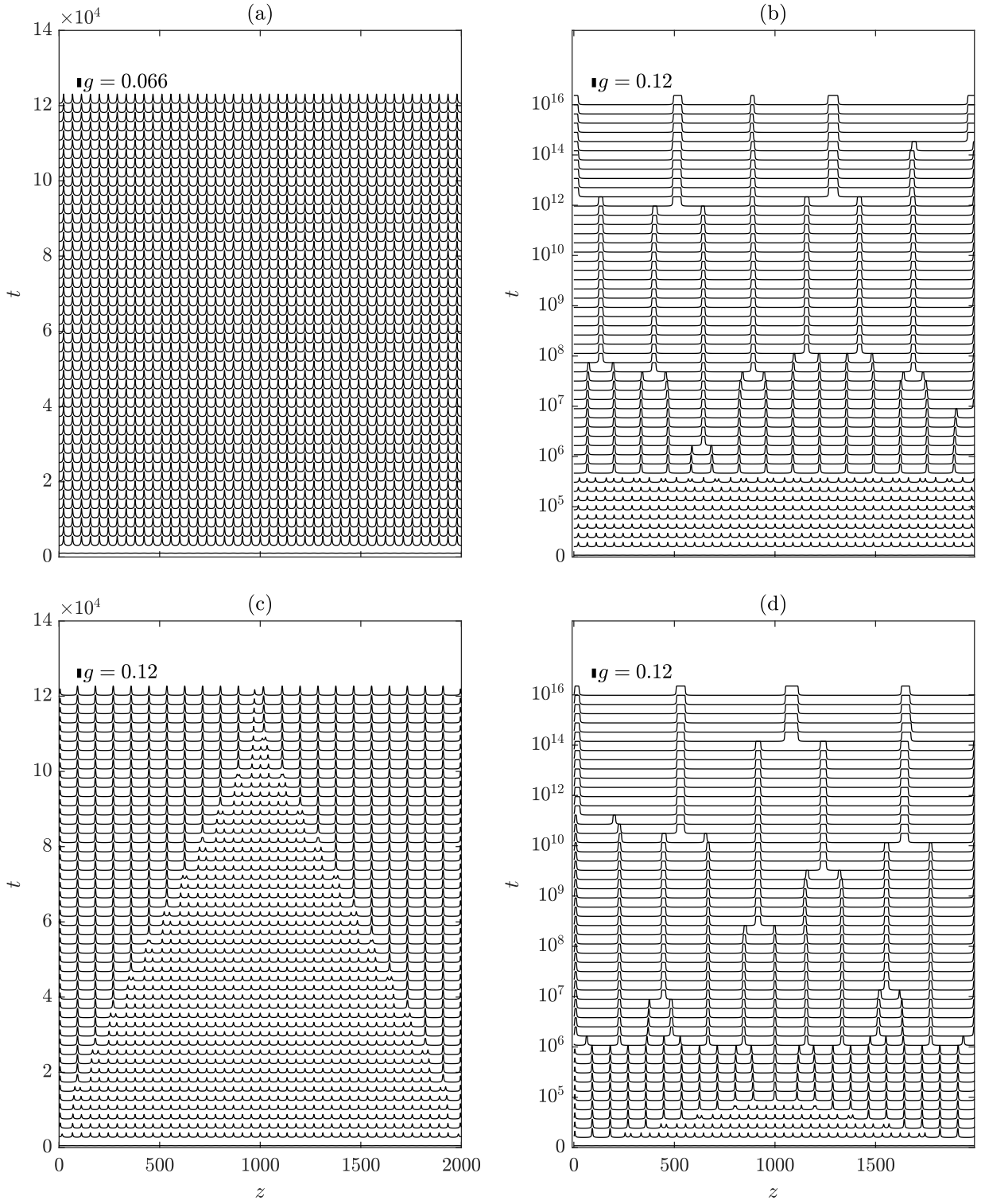


FIG. 7. Time evolution of the buoyancy gradient $g(z, t) = b_z(z, t)$ for fixed-buoyancy boundary conditions (40), and initial conditions (44)–(45) with wavenumber $n = 45$, background buoyancy gradient $g_0 = 0.0218$, dissipation parameter $r = 50$, and domain thickness $H = 2000$. Zero-energy-flux boundary conditions (41) are adopted in (a) and (b); fixed energy conditions (42) are adopted in (c) and (d). The scale bar at the top left of each panel indicates the magnitude of the gradient $g(z, t)$.

The key conclusion to be drawn is that, for fixed-buoyancy boundary conditions, the evolution of layers is largely unaffected by the boundaries (except at early times, in the case of fixed-energy boundary conditions). The layered region evolves independently through merger events until a single interface remains in the middle of the domain. This behaviour differs from the situation of BLY, where edge regions moved into the interior (cf. Fig. 2), gradually engulfing the layers until a uniform state exists across the entire domain. Further numerical simulations with more complex initial conditions show that even for initial conditions that do produce edge regions, fixed-buoyancy boundary conditions prevent the intrusion of the edge regions into the interior.

B. Evolution to late times

We now turn our attention to the long-term nonlinear evolution of solutions to the full system (26)–(28), for non-zero values of Pe^{-1} and Re^{-1} . As discussed in Sec. IV A, we take boundary conditions (40) and (41) to prevent the development of expanding edge regions and provide a clean framework in which to analyse the dynamics of layers. For the buoyancy, we take initial condition (44), namely a uniform buoyancy gradient perturbed by the wavenumber of maximum growth rate. For numerical convenience, we initialise the energy with the steady state energy corresponding to $Pe^{-1} = 0$ — this is appropriate because the values of Pe^{-1} that we consider are sufficiently small that the true steady-state energy is close to the energy for $Pe^{-1} = 0$. In the numerical solutions, the energy adjusts rapidly to its true steady-state value.

One aim of our numerical simulations is to demonstrate how the predicted wavenumbers of maximum growth rate, and the growth rates themselves, are manifest in the nonlinear solutions; these predictions are detailed in Table II. First, we show solutions for parameters relevant to typical temperature- and salt-stratified water at $Re^{-1} = 0.1$. Next, we consider two choices of parameters that predict, and produce, significantly fewer layers, thereby demonstrating the behaviour of larger-scale layers and interfaces. We conclude this section by investigating the trends in the long-term evolution of layers and the occurrence of mergers, inferring a general law describing the number of interfaces with time.

In Sec. III C, we showed the effects of changing parameter values on the initial development of layers. Figure 8 demonstrates the effects of changing Pe^{-1} and Re^{-1} on solutions of (26)–(28), for values chosen from Table II. In each case, we take the dissipation parameter $r = 50$, and choose the background buoyancy gradient to be $g_0 = 0.0218$. This value of g_0 is chosen to be approximately in the middle of the unstable range of buoyancy gradients predicted for this value of r , for a wide range of choices of Pe^{-1} , as seen in Fig. 4(b).

Figure 8(a) shows a typical temperature-stratified case with $Pe^{-1} = 0.01$ and $Re^{-1} = 0.1$, chosen such that $Pr = Pe/Re = 10$. In the initial condition (44), we take $n = 40$, giving a predicted linear growth rate of 1.15×10^{-3} . The initial perturbation grows into a series of 40 layers across the entire fluid depth, which undergo a set of mergers by $t \approx 0.5 \times 10^6$. Successive merger events take place, until there are four interfaces remaining by $t = 10^{18}$. The maximum gradient in an interface (shown in the plot as the height of a spike) is initially $g = 0.056$, increasing to $g = 0.91$ in the first set of mergers. After the first mergers are complete, successive mergers do not increase the maximum gradient, but instead create thicker interfaces, conserving the total density difference across an interface following a merger.

Figure 8(b) shows a typical salt-stratified case with $Pe^{-1} = 0.0001$ and $Re^{-1} = 0.1$, such that $Sc = Pe/Re = 1000$. Here we take $n = 43$ in the initial condition (44), giving a growth rate of 1.5×10^{-3} , approximately one and a half times greater than that in the temperature-stratified case shown in Fig. 8(a). The system initially develops into 43 layers, which merge by $t \approx 0.9 \times 10^6$, taking almost twice as long as for the temperature-stratified case. Thus, the increased linear growth rate of perturbations does not imply that mergers happen more quickly. The maximum interfacial gradient is initially $g = 0.064$, increasing to $g = 0.12$ after the first mergers — these gradients are both slightly larger than for the temperature-stratified case, reflecting the fact that smaller values of Pe^{-1} give a larger range of unstable buoyancy gradients in the linear analysis of Sec. III B.

Figures 8(c,d) show the evolution of the system for parameter choices that produce significantly smaller wavenumbers of maximum growth rate. In both cases we take $Re^{-1} = 1$. Figure 8(c) has $Pe^{-1} = 0.001$, which predicts a wavenumber of maximum growth rate corresponding to $n = 24$. Here, the evolution resembles that in Figs. 8(a,b), with the main difference being the initial number of layers. The predicted growth rate is 5×10^{-4} , approximately half that for the temperature-stratified case. The first set of mergers is complete by $t \approx 4 \times 10^5$ — similar to both Figs. 8(a,b), demonstrating again that the linear growth rate cannot be used to predict a timescale for mergers. Figure 8(d) has $Pe^{-1} = 0.1$, giving $n = 6$ as the most unstable wavenumber. The linear growth rate of 2.6×10^{-6} is significantly smaller than in any of the other plots, and clear layers are not apparent until $t > 10^6$. The first mergers occur at $t \approx 10^8$. The interfaces are very thick, with small gradients: the maximum interfacial gradient is $g = 0.03$, a factor of three smaller than for the cases shown in Figs. 8(a–c).

The plots in Fig. 9 show how the interfaces change over long timescales; they are derived from several numerical

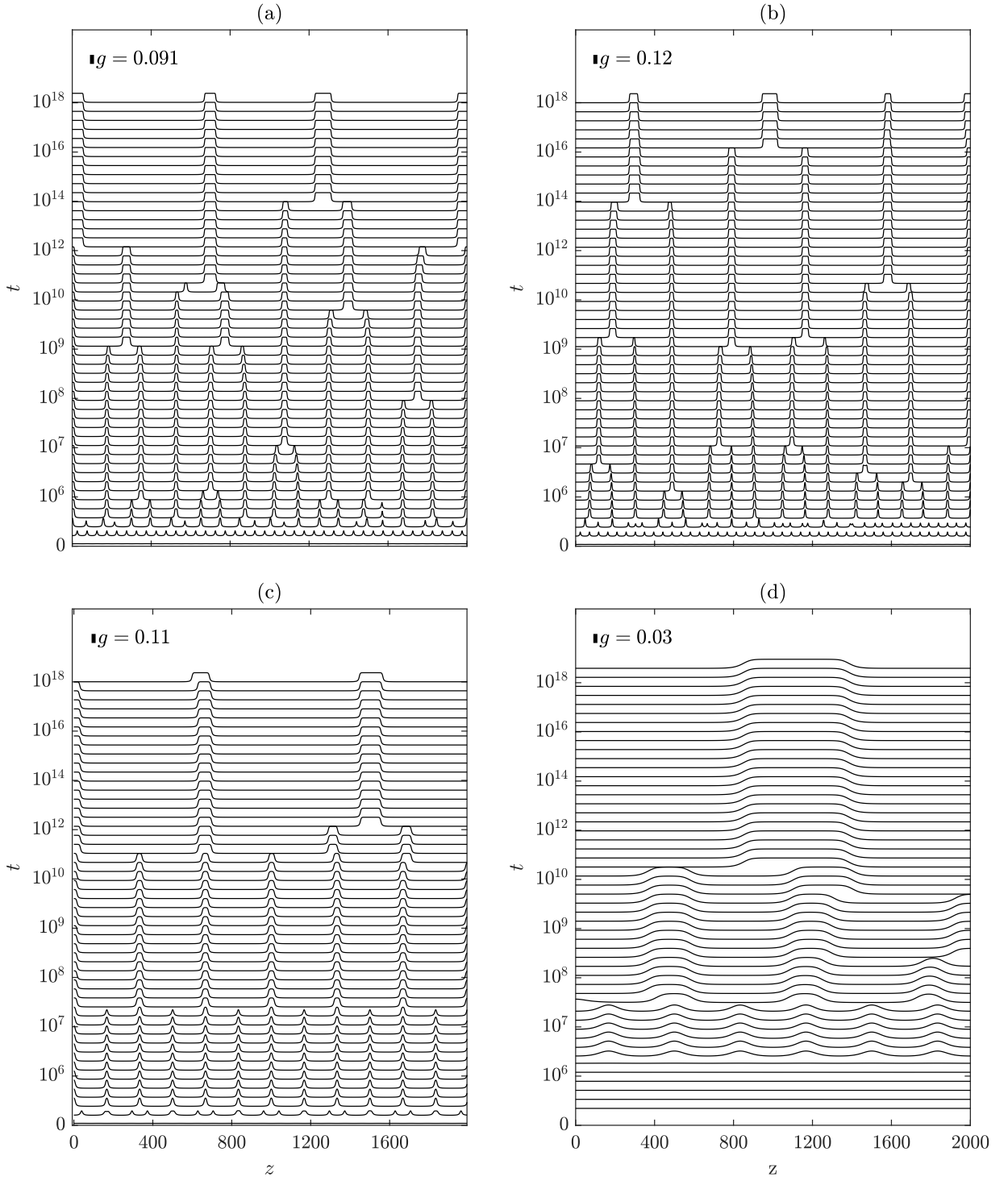


FIG. 8. Long-time evolution of the buoyancy gradient $g(z, t)$, resulting from solution of the system (26)–(28) with diffusion included; in the basic state $g_0 = 0.0218$. Panel (a) shows a typical temperature-stratified case with $Pe^{-1} = 0.01$, $Re^{-1} = 0.1$, and $n = 40$ initial interfaces; (b) a typical salt-stratified case with $Pe^{-1} = 0.0001$, $Re^{-1} = 0.1$, $n = 43$; (c) $Pe^{-1} = 0.001$, $Re^{-1} = 1$, $n = 24$; (d) $Pe^{-1} = 0.1$, $Re^{-1} = 1$, $n = 6$. In each case, the dissipation parameter $r = 50$. The scale bar at the top left of each panel indicates the magnitude of the gradient $g(z, t)$.

simulations across a range of parameters chosen to cover the full unstable range shown in Fig. 4(b). The parameters used to produce these results are given in Table III. Figure 9(a) shows the maximum buoyancy gradient across the whole solution at each time; this corresponds to the gradient at the centre of the sharpest interfaces (and is representative of all interfaces). Figure 9(b) shows how the number of interfaces decreases with time; merger events can be seen as sharp downward steps in the profiles. In Fig. 9(a), the early phase of the evolution is marked by a smooth increase in the gradient from the initial perturbation to a value at which the first interfaces appear. The maximum gradient then remains unchanged for a prolonged period, until the first mergers occur. At this point, the maximum gradient increases sharply before settling again at a new value. In most cases, this second increase in gradient has approximately the same magnitude as the first. However, for the red and yellow lines (beginning at $\max(b_z) = 0.015$ and 0.8 respectively) the second increase is significantly smaller. Once the stable maximum gradient is reached, it remains unchanged, even with further mergers, as can be seen by comparison of Figs. 9(a,b). However, the density difference across two merging interfaces must be conserved, so the remaining interface is thicker than either of the two interfaces that formed it. This increase in interface thickness can be seen clearly in Figs. 8(a–d).

In Fig. 9(b), each solid line begins at the time when the initial layered state is fully formed (corresponding to the end of the first step up in Fig. 9(a)), and tracks the number of interfaces, including those on the boundaries. The interfaces are determined by locating all peaks in the buoyancy gradient with a magnitude above a critical value, chosen to be the steady gradient of the initial interfaces seen in Fig. 9(a). BLY briefly state that the timescale for successive mergers ‘becomes exponentially long’. However, the expanding edge regions in their solutions prevent a thorough investigation of long-term merger behaviour. Our choice of boundary conditions allows us to examine the long-term evolution of the solutions and, in turn, quantify this dependence more precisely. In Fig. 9(b), the dashed lines are fitted according to a least squares regression, and show a good fit with the general relation

$$\frac{1}{N} \sim \alpha \log t + \beta, \quad (46)$$

representing an inverse logarithmic dependence for the number of layers over time, $N(t)$. As shown in Fig. 9, the relation (46) captures the overall trend for $N(t)$ over several orders of magnitude of time, potentially indicating a self-similar structure to successive layer mergers. Expression (46) indicates the existence of a general law for how interfaces in stratified turbulence evolve, with the coefficients α and β dependent on the viscosity and diffusivity of the fluids. Values of α and β for each case are given in Table III. Analysis of layering in the Cahn-Hilliard equation has demonstrated such a logarithmic timescale [27], which has been confirmed by several numerical studies (e.g. [33, 34]). BLY showed that their model could be transformed into the Cahn-Hilliard equation through an asymptotic analysis about the point of marginal stability in g_0 - r space (the tip of the black curve in Fig. 4(b)). Figure 9(b) demonstrates such a logarithmic timescale across the entire unstable range of parameters, confirming the relevance of Cahn-Hilliard dynamics to models of layering that employ the Phillips effect.






Line	r	Pe^{-1}	Re^{-1}	H	n	α	β
	50	0.01	0.1	2000	40	0.0080	-0.059
	100	0.1	0.1	2000	12	0.015	-0.098
	15	0	0	2000	15	0.011	-0.044
	50	0.01	0.1	6000	119	0.0027	-0.018
	50	0.001	0.1	4000	87	0.0037	-0.022

TABLE III. Parameter values for the plots in Fig. 9, and corresponding values of α and β for the trend law (46).

V. DISCUSSION

In this paper we have made four primary developments in the analysis of layering in stratified turbulent flow. First, we have presented a general horizontally averaged model derived from the Boussinesq equations using a spatial averaging approach. Our formulation retains the effects of viscosity and molecular diffusivity, and explicitly clarifies the closure assumptions required. Second, we have demonstrated how the layering instability is affected by molecular diffusivity and viscosity. Third, we have demonstrated the importance of boundary conditions on the long-term evolution of the solutions. Finally, we have shown how the long-term distribution of layers changes through merger events, with the inference of a general power law dependence describing the number of layers as a function of time.

In order to understand the essential conditions for layer formation, we investigated the linear stability of uniform gradient, uniform energy steady states. Increasing Pe^{-1} suppresses the instability by decreasing the range of unstable gradients. Increasing Re^{-1} does not affect which gradients lead to instability, but does decrease the range of unstable

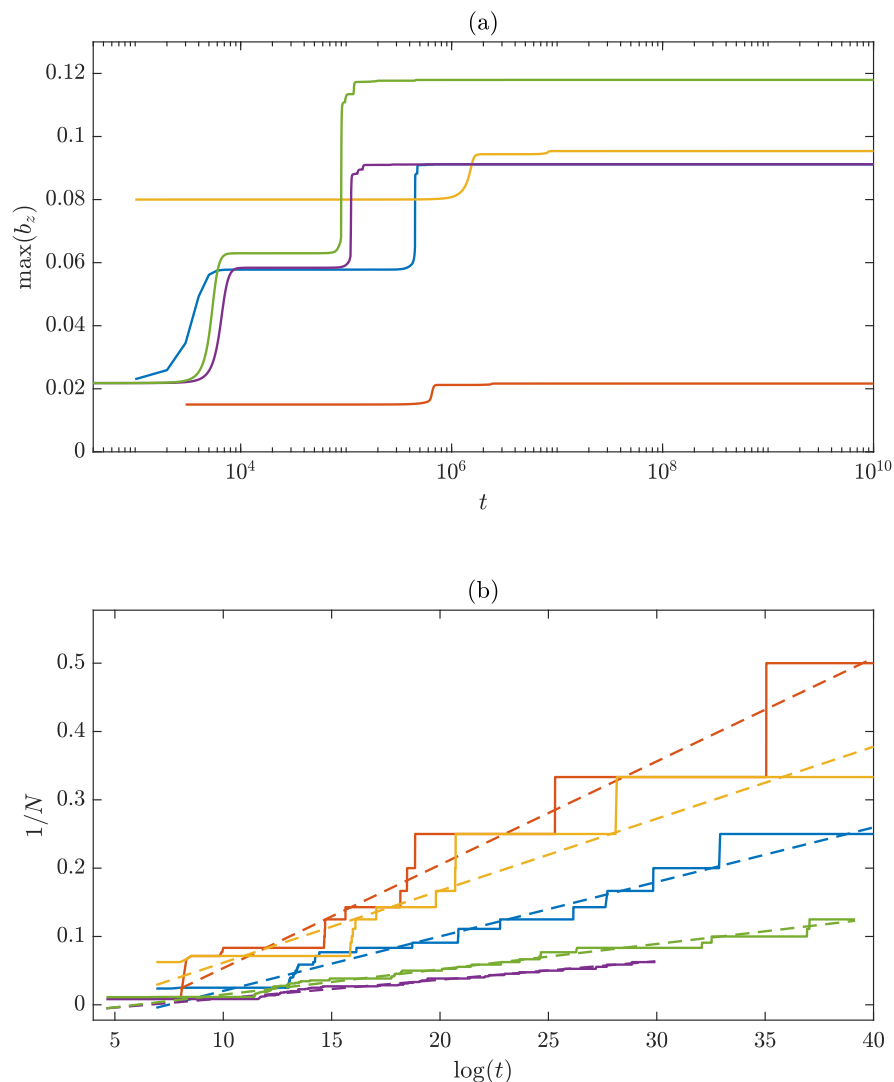


FIG. 9. Plots showing variation in the interfaces over time. Panel (a) shows the maximum gradient at each time, corresponding to the gradient at the centre of the sharpest interface. Panel (b) shows the number of interfaces at each time, plotted against $\log(t)$. The dashed lines show the best fits to relation (46). The parameters used for each curve are reported in Table III.

wavenumbers, so the instability occurs only at larger scales. Since for temperature-stratified water, Pe^{-1} is two orders of magnitude larger than for salt-stratified water, the latter is more susceptible to layering.

We have shown that fixed-buoyancy boundary conditions ensure that the layered regions extend across the entire depth of the domain for all time. This contrasts with the case of fixing the buoyancy gradient, which allows layer-free edge regions to expand into the interior, gradually engulfing the layers [20]. In our numerical solutions, multiple layer merger events take place in groups, with the general property that the maximum gradient across an interface approximately doubles after the first group of mergers. In subsequent mergers, the gradient does not increase further. Instead, the thicknesses of the interfaces increase, conserving the total density difference across the interface. Our analysis of the solutions over long times shows that after the initial development of layers, the number of interfaces conforms to the law $1/N \sim \log t$, thereby generalising the link to Cahn-Hilliard dynamics shown by BLY.

To expand on this work, we plan to test the predictions experimentally. Previous experimentation [2, 3] has shown that layering occurs above a critical Richardson number (defined as $Ri = N^2 d^2 / U^2$, where U and d are the speed and scale of a stirring rod, and N the Brunt-Väisälä frequency of the stratification). Note that with all other parameters fixed, Ri is proportional to the buoyancy gradient $g = b_z$. Hence, a minimum Richardson number is tantamount to a single critical value of the buoyancy gradient g above which layering takes place. In addition to this lower bound, our work has illustrated the possibility of a maximum buoyancy gradient above which layering does not occur. This property, which arises because a sufficiently strong gradient will suppress the instability, remains to be demonstrated

experimentally. An experimental investigation into these critical conditions on both maximum and minimum gradients for layer development could also be used to constrain the model parameters, such as the dissipation coefficient r .

Our analysis and derivation of a horizontally-averaged model provides a basis for generalisation to other systems in which layering occurs. In particular, the two-component model for buoyancy and energy can be expanded to a double-diffusive system by the inclusion of an additional equation for the second component of buoyancy. This produces a three-component model for temperature and salinity (or any other two components of density), and energy. Two specific problems suggest themselves. The first is to study a three-component model with an external forcing, as used here. This will provide insights into the second problem, in which the turbulent motions arise naturally from the convective instability of the basic state; here, the prescription of the mixing length in the ‘stirred’ state becomes the crucial issue. This work is ongoing and will be reported in a future paper.

PP is supported by the Natural Environment Research Council Panorama DTP [Grant No. NE/S007458/1]. We are grateful to participants at the KITP Staircase 21 Programme, [National Science Foundation Grant No. NSF PHY-1748958] for helpful discussions. In addition, DWH thanks Pat Diamond for useful discussions. We also thank the referees for their insightful reports that helped improve the paper.

-
- [1] P. F. Linden. Mixing in stratified fluids. *Geophys. Astrophys. Fluid Dyn.*, 13:3–23, 1979.
- [2] B. R. Ruddick, T. J. McDougall, and J. S. Turner. The formation of layers in a uniformly stirred density gradient. *Deep Sea Res A*, 36:597–609, 1989.
- [3] Y. Park, J. A. Whitehead, and A. Gnanadeskian. Turbulent mixing in stratified fluids: layer formation and energetics. *J. Fluid Mech.*, 279:279–311, 1994.
- [4] P. S. Marcus. Jupiter’s Great Red Spot and other vortices. *Ann. Rev. Astron. Astrophys.*, 31:523–573, 1993.
- [5] D. G. Dritschel and M. E. McIntyre. Multiple jets as PV staircases: the Phillips effect and the resilience of eddy-transport barriers. *J. Atmos. Sci.*, 65:855–874, 2008.
- [6] R. W. Schmitt, J. R. Ledwell, E. T. Montgomery, K. L. Polzin, and J. M. Toole. Enhanced diapycnal mixing by salt fingers in the thermocline of the tropical Atlantic. *Science*, 308:685–688, 2005.
- [7] M. L. Timmermans, J. Toole, A. Proshutinsky, R. Krishfield, and A. Plueddemann. Eddies in the Canada Basin, Arctic Ocean, observed from ice-tethered profilers. *J. Phys. Oceanogr.*, 38:133, 2008.
- [8] T. Radko. A mechanism for layer formation in a double-diffusive fluid. *J. Fluid Mech.*, 497:365–380, 2003.
- [9] S. Stellmach, A. Traxler, P. Garaud, N. Brummell, and T. Radko. Dynamics of fingering convection. Part 2 The formation of thermohaline staircases. *J. Fluid Mech.*, 677:554–571, 2011.
- [10] E. Rosenblum, P. Garaud, A. Traxler, and S. Stellmach. Turbulent mixing and layer formation in double-diffusive convection: three-dimensional numerical simulations and theory. *Astrophys. J.*, 731:66, 2011.
- [11] D. W. Hughes and N. H. Brummell. Double-diffusive magnetic layering. *Astrophys. J.*, 922:195, 2021.
- [12] G. Dif-Pradalier, P. H. Diamond, V. Grandgirard, Y. Sarazin, J. Abiteboul, X. Garbet, Ph. Ghendrih, A. Strugarek, S. Ku, and C. S. Chang. On the validity of the local diffusive paradigm in turbulent plasma transport. *Phys. Rev. E*, 82:02540-1, 2010.
- [13] G. Dif-Pradalier, G. Hornung, P. Ghendrih, Y. Sarazin, F. Claret, L. Vermare, P. H. Diamond, J. Abiteboul, T. Cartier-Michaud, C. Ehrlacher, D. Estève, X. Garbet, V. Grandgirard, Ö. D. Gürçan, P. Hennequin, Y. Kosuga, G. Latu, P. Maget, P. Morel, C. Norscini, R. Sabot, and A. Storelli. Finding the elusive $\mathbf{E} \times \mathbf{B}$ staircase in magnetized plasmas. *Phys. Rev. Lett.*, 114:085004, 2015.
- [14] O. M. Phillips. Turbulence in a strongly stratified fluid—is it unstable? *Deep Sea Res.*, 19:79 – 81, 1972.
- [15] E. S. Posmentier. The generation of salinity finestructure by vertical diffusion. *J. Phys. Oceanogr.*, 7:298–300, 1977.
- [16] J. G. Fitzgerald and B. F. Farrell. Statistical state dynamics analysis of buoyancy layer formation via the Phillips mechanism in two-dimensional stratified turbulence. *J. Fluid Mech.*, 864, 2019.
- [17] Y. Ma and W. R. Peltier. Thermohaline staircase formation in the diffusive convection regime: a theory based upon stratified turbulence asymptotics. *J. Fluid Mech.*, 931, 2022.
- [18] G. I. Barenblatt, M. Bertsch, R. Dal Passo, V. M. Prostokishin, and M. Ughi. A mathematical model of turbulent heat and mass transfer in stably stratified shear flow. *J. Fluid Mech.*, 253:341–358, 1993.
- [19] Y. Kosuga, P. H. Diamond, and Ö. D. Gürçan. How the propagation of heat-flux modulations triggers $\mathbf{E} \times \mathbf{B}$ flow pattern formation. *Phys. Rev. Lett.*, 110(10):105002, 2013.
- [20] N. J. Balmforth, S. G. Llewellyn Smith, and W. R. Young. Dynamics of interfaces and layers in a stratified turbulent fluid. *J. Fluid Mech.*, 355:329–358, 1998.
- [21] R. V. Ozmidov. On the turbulent exchange in a stably stratified ocean. *Izv. Acad. Sci. USSR. Atmos. Oceanic Phys.*, 1:861–871, 1965.
- [22] F. Paparella and J. von Hardenberg. A model for staircase formation in fingering convection. *Acta Appl. Math.*, 132:457–467, 2014.
- [23] M. A. Malkov and P. H. Diamond. Dynamics of potential vorticity staircase evolution and step mergers in a reduced model of beta-plane turbulence. *Phys. Rev. Fluids*, 4:044503, 2019.
- [24] A. Ashourvan and P. H. Diamond. How mesoscopic staircases condense to macroscopic barriers in confined plasma

- turbulence. *Phys. Rev. E*, 94:05120-2, 2016.
- [25] A. Ashourvan and P. H. Diamond. On the emergence of macroscopic transport barriers from staircase structures. *Phys. Plasmas*, 24:01230-5, 2017.
- [26] W. Guo, P. H. Diamond, D. W. Hughes, L. Wang, and A. Ashourvan. Scale selection and feedback loops for patterns in drift wave-zonal flow turbulence. *Plasma Phys. Control. Fusion*, 61:105002, 2019.
- [27] T. Kawakatsu and T. Munakata. Kink dynamics in a one-dimensional conserved TDGL system. *Prog. Theor. Phys.*, 74:11–19, 1985.
- [28] N. J. Balmforth and Y-N. Young. Stratified Kolmogorov Flow. Part 2. *J. Fluid Mech.*, 528:23–42, 2005.
- [29] W. P. Jones and B. E. Launder. The prediction of laminarization with a two-equation model of turbulence. *Intl. J Heat Mass Transf.*, 15:301–314, 1972.
- [30] K. G. Nayar, M. H. Sharqawy, L. D. Banchik, et al. Thermophysical properties of seawater: A review and new correlations that include pressure dependence. *Desalination*, 390:1–24, 2016.
- [31] M. H. Sharqawy, J. H. Lienhard, and S. M. Zubair. Thermophysical properties of seawater: a review of existing correlations and data. *Desalination Water Treat.*, 16:354–380, 2010.
- [32] N. Ramsing and J. Gunderson. Unisense seawater and gases table. <https://www.unisense.com/files/PDF/Diverse/Seawater%20&%20Gases%20table.pdf>.
- [33] T. Nagai and K. Kawasaki. Molecular dynamics of interacting kinks. I. *Physica A*, 120:587–599, 1983.
- [34] S. J. Watson, F. Otto, B. Y. Rubinstein and S. H. Davis. Coarsening dynamics of the convective Cahn-Hilliard equation. *Physica D*, 178:127–148, 2003.